An arbitrary high-order discontinuous Galerkin method for elastic waves on unstructured meshes – I. The two-dimensional isotropic case with external source terms

Martin Käser and Michael Dumbser

Department of Civil and Environmental Engineering, University of Trento, Trento, Italy. E-mail: martin.kaeser@ing.unitn.it

SUMMARY

We present a new numerical approach to solve the elastic wave equation in heterogeneous media in the presence of externally given source terms with arbitrary high-order accuracy in space and time on unstructured triangular meshes. We combine a discontinuous Galerkin (DG) method with the ideas of the *ADER* time integration approach using *A*rbitrary high-order *DER*ivatives. The time integration is performed via the so-called Cauchy-Kovalewski procedure using repeatedly the governing partial differential equation itself. In contrast to classical finite element methods we allow for discontinuities of the piecewise polynomial approximation of the solution at element interfaces. This way, we can use the well-established theory of fluxes across element interfaces based on the solution of Riemann problems as developed in the finite volume framework. In particular, we replace time derivatives in the Taylor expansion of the time integration procedure by space derivatives to obtain a numerical scheme of the same high order in space *and* time using only one single explicit step to evolve the solution from one time level to another. The method is specially suited for linear hyperbolic systems such as the heterogeneous elastic wave equations and allows an efficient implementation. We consider continuous sources in space and time and point sources characterized by a Delta distribution in space and some continuous source time function. Hereby, the method is able to deal with point sources at *any* position in the computational domain that does not necessarily need to coincide with a mesh point. Interpolation is automatically performed by evaluation of test functions at the source locations. The convergence analysis demonstrates that very high accuracy is retained even on strongly irregular meshes and by increasing the order of the ADER–DG schemes computational time and storage space can be reduced remarkably. Applications of the proposed method to Lamb's Problem, a problem of strong material heterogeneities and to an example of global seismic wave propagation finally confirm its accuracy, robustness and high flexibility.

Key words: arbitrary high order, discontinuous Galerkin method, elastic waves, unstructured mesh.

1 INTRODUCTION

The accurate simulation of elastic wave propagation in heterogeneous media with complicated geometry is still a challenging task. Unstructured meshes that can be adapted to difficult geometrical models often lead to less accurate numerical schemes. However, as the waveforms contain important information about the interior structure of a material, it is necessary to develop numerical methods that are capable of computing accurate solutions, for example, seismograms of high frequencies, even on such strongly irregular meshes that may arise when complex geometries have to be meshed. Furthermore highly accurate numerical schemes serve to eliminate as far as possible the errors introduced purely by the numerical approximation of the underlying physical model such that the misfit of simulated and measured data should only be due to errors in the mathematical description of the physical problem or due to incorrect initialization of the physical parameters of the investigated model and not due to insufficient accuracy of the numerical method that is used.

In the past two decades a variety of different numerical schemes has been developed in order to solve the elastic wave equations. Finite difference (FD) schemes for the simulation of *SH* and *P–SV* waves on regular, staggered grids were introduced by Madariaga (1976) and Virieux (1984, 1986). Later these schemes were extended for instance to higher orders (Levander 1988), to three dimensions (Mora 1989;

855

GJI Seismology

Moczo *et al.* 2002) and anisotropic material (Igel *et al.* 1995; Tessmer 1995) to give just a partial list. FD like methods on unstructured meshes were developed in (Käser & Igel 2001a,b).

Alternatively pseudo-spectral methods (Fornberg 1996) have been developed, for example, by Carcione (1994) and applied in (Tessmer & Kosloff 1994; Igel 1999), where the space dependent variables are expanded in a set of orthogonal basis functions which are known exactly at discrete locations and which also allow the accurate computation of derivatives. Furthermore, no grid-staggering is needed, which provides advantages when modeling anisotropic material. However, quite regular meshes have to be used and due to the global character of the derivative operators parallelization is cumbersome.

Recently the spectral element method (SEM), originally introduced by Patera (1984) in the field of computational fluid mechanics, gained increasing popularity in numerical seismology. SEM for elastic wave propagation has been applied in two and three space dimensions (Priolo *et al.* 1994; Komatitsch & Vilotte 1998; Seriani 1998) and demonstrated advantages in particular for the problem of global wave propagation (Komatitsch & Tromp 1999, 2002). The fundamental idea is to combine the advantages of a spectral method with those of a finite element (FE) method.

However, it is worth mentioning that all the above mentioned schemes usually use rather low-order schemes for the time integration, for example, second-order Newmark-type schemes (Hughes 1987) or at most fourth-order Runge-Kutta schemes, for example, (Igel 1999). Even though these former schemes have proven to be very successful, for example, (Thompson & Pinsky 1996), we note that for wave propagation problems, where waves are propagating over many wavelengths, time accuracy is crucial, especially when very high accuracy is required. We confirm this statement by the numerical convergence analysis in this work and also refer to results shown in (Dumbser *et al.* 2005).

Therefore, in this paper we present a new discontinuous Galerkin (DG) FE scheme for two space dimensions that uses the arbitrary high-order derivatives (ADER) approach in order to solve the elastic wave equations with very high accuracy in both space *and* time. The proposed numerical method relies on the combination of the Discontinuous Galerkin FE method and the ADER approach, originally developed by Toro *et al.* (2001) and Titarev & Toro (2002) and in (Schwartzkopff *et al.* 2002, 2004) in the finite volume (FV) framework. The DG schemes belong to new class of numerical methods first used by Reed & Hill (1973) to solve linear neutron transport equations. As usual in the FE framework, the unknown solution is approximated inside each element by a polynomial, whose coefficients—the degrees of freedom—are advanced in time. In contrast to classical continuous FE, within the DG framework the solution can be *discontinuous* across the element interfaces, which allows the incorporation the well-established ideas of numerical flux functions from the FV framework. In the last decade mainly Cockburn & Shu (1989a, 1989b, 1990, 1991, 1998) put the DG schemes into a clear framework together with total variation diminishing (TVD) Runge-Kutta time integration methods.

Here, we present a theoretically arbitrary high-order DG scheme in combination with the ADER approach in order to reach space and time accuracy of the same order. Furthermore, the method is formulated as a one step scheme, that is, we do not need to compute and store intermediate stages as, for example, for Runge-Kutta methods to update the solution to the successive time level. The ADER–DG method proposed in this paper can handle unstructured triangular meshes and, therefore, is extremely flexible as far as computational domains with complicated geometrical structure are concerned. ADER–DG schemes were first developed for linear hyperbolic systems with constant coefficients or for linear systems with variable coefficients in conservative form (Dumbser & Munz 2005a,b).

In this paper we consider the extension to non-conservative systems with variable coefficients such as the heterogeneous elastic wave equation.

The paper is structured as follows. In Section 2 we introduce the system of the elastic wave equations in the non-conservative velocity-stress formulation including external source term depending on space and time. The proposed DG scheme is presented in Section 3 together with the ADER time integration approach and an efficient formulation of the required Cauchy-Kovalewski procedure. In Section 4 we address the conditions for absorbing and free surface boundaries. After investigating numerically the convergence of the ADER–DG scheme with and without source terms in Section 5 on regular and very irregular triangular meshes, we show applications of the new scheme in Section 6. The first considers Lamb's Problem to validate the correct treatment of points sources and free surface boundaries. The second test case investigates strong material heterogeneities as suggested by LeVeque (2002) and the last example solves the problem of global, 2-D wave propagation using the radially symmetric preliminary reference earth model (PREM) of Dziewonski & Anderson (1981).

2 ELASTIC WAVE EQUATIONS

The propagation of waves in an elastic medium is based on the theory of linear elasticity (Aki & Richards 2002; Bedford & Drumheller 1994). Combining the definition of strain caused by deformations (Hooke's law) and the equations of the dynamic relationship between acceleration and stress, the elastic wave equations can be derived as shown in (LeVeque 2002). Considering the 2-D elastic wave equation for an isotropic medium in velocity-stress formulation and admitting external sources (e.g. moments or body forces) leads to a linear hyperbolic system of the form

$$\frac{\partial}{\partial t}\sigma_{xx} - (\lambda + 2\mu)\frac{\partial}{\partial x}v - \lambda\frac{\partial}{\partial y}w = S_1(x, y, t),$$

$$\frac{\partial}{\partial t}\sigma_{yy} - \lambda\frac{\partial}{\partial x}v - (\lambda + 2\mu)\frac{\partial}{\partial y}w = S_2(x, y, t),$$

$$\frac{\partial}{\partial t}\sigma_{xy} - \mu\left(\frac{\partial}{\partial x}w + \frac{\partial}{\partial y}v\right) = S_3(x,y,t),$$

$$\rho\frac{\partial}{\partial t}v - \frac{\partial}{\partial x}\sigma_{xx} - \frac{\partial}{\partial y}\sigma_{xy} = \rho S_4(x,y,t),$$

$$\rho\frac{\partial}{\partial t}w - \frac{\partial}{\partial x}\sigma_{xy} - \frac{\partial}{\partial y}\sigma_{yy} = \rho S_5(x,y,t),$$ (1)

where λ and μ are the *Lamé constants* and ρ is the mass density of the material. The normal stress components are given by σ_{xx} and σ_{yy}, and the shear stress is σ_{xy}. The components of the particle velocities in x- and y-direction are denoted by v and w, respectively. $S_p(x,y,t)$, $p = 1,\ldots,5$, is the vector of space–time dependent source terms. This system was already used in the seminal papers of Virieux (1984, 1986), however, only for the homogeneous case, where $S_p = 0$ for $p = 1,\ldots,5$.

We remark that for notational simplicity, we skip the time and space dependencies of the variables. For the rest of this paper, the stresses and velocities are always assumed to be functions of time and space, that is, $\sigma_{xx} = \sigma_{xx}(\vec{x},t)$, $\sigma_{yy} = \sigma_{yy}(\vec{x},t)$, $\sigma_{xy} = \sigma_{xy}(\vec{x},t)$, $v = v(\vec{x},t)$, $w = w(\vec{x},t)$, with $t \in \mathbb{R}$ and $\vec{x} = (x,y)^T \in \mathbb{R}^2$. The physical properties of the material are functions of space but are constant in time, that is, $\lambda = \lambda(\vec{x})$, $\mu = \mu(\vec{x})$, and $\rho = \rho(\vec{x})$.

For the following investigation of the eigenstructure of the system (1), we use the more compact form

$$\frac{\partial u_p}{\partial t} + A_{pq}\frac{\partial u_q}{\partial x} + B_{pq}\frac{\partial u_q}{\partial y} = S_p,$$ (2)

where u is the vector of the p unknown variables, that is, $u = (\sigma_{xx}, \sigma_{yy}, \sigma_{xy}, v, w)^T$ and S_p is the space–time-dependent source vector. We use classical tensor notation, which implies summation over each index appearing twice. The matrices $A_{pq} = A_{pq}(\vec{x})$ and $B_{pq} = B_{pq}(\vec{x})$ are the space dependent Jacobian matrices of size $p \times q$, with $p,q = 1,\ldots,5$, as given by

$$A_{pq} = \begin{pmatrix} 0 & 0 & 0 & -(\lambda+2\mu) & 0 \\ 0 & 0 & 0 & -\lambda & 0 \\ 0 & 0 & 0 & 0 & -\mu \\ -\frac{1}{\rho} & 0 & 0 & 0 & 0 \\ 0 & 0 & -\frac{1}{\rho} & 0 & 0 \end{pmatrix},$$ (3)

$$B_{pq} = \begin{pmatrix} 0 & 0 & 0 & 0 & -\lambda \\ 0 & 0 & 0 & 0 & -(\lambda+2\mu) \\ 0 & 0 & 0 & -\mu & 0 \\ 0 & 0 & -\frac{1}{\rho} & 0 & 0 \\ 0 & -\frac{1}{\rho} & 0 & 0 & 0 \end{pmatrix}.$$ (4)

In the framework of unstructured triangular meshes, where element edges in general are not aligned with the coordinate axis, the Jacobian matrix $(A_n)_{pq}$ in normal direction $\vec{n} = (n_x, n_y)^T$ to a element interface is obtained by the linear combination of the Jacobian matrices in eqs (3) and (4)

$$(A_n)_{pq} = n_x A_{pq} + n_y B_{pq}$$

$$= \begin{pmatrix} 0 & 0 & 0 & -n_x(\lambda+2\mu) & -n_y\lambda \\ 0 & 0 & 0 & -n_x\lambda & -n_y(\lambda+2\mu) \\ 0 & 0 & 0 & -n_y\mu & -n_x\mu \\ -\frac{n_x}{\rho} & 0 & -\frac{n_y}{\rho} & 0 & 0 \\ 0 & -\frac{n_y}{\rho} & -\frac{n_x}{\rho} & 0 & 0 \end{pmatrix}.$$ (5)

The propagation velocity of the elastic waves are determined by the eigenvalues of the Jacobian matrices A_{pq} and B_{pq} and result in

$$s_1 = -c_p, \quad s_2 = -c_s, \quad s_3 = 0, \quad s_4 = c_s, \quad s_5 = c_p,$$ (6)

where

$$c_p = \sqrt{\frac{\lambda+2\mu}{\rho}}, \quad \text{and} \quad c_s = \sqrt{\frac{\mu}{\rho}}.$$ (7)

We remark that for the isotropic case the wave speeds in eqs (6) and (7) do not depend on the propagation direction. The two P waves propagate with speeds s_1 and s_5 and the two S waves propagate with speeds s_2 and s_4 in the negative and positive direction with respect to $\vec{n}$.

$R_{p1}^{A_n}, \ldots, R_{p5}^{A_n}$ denote the right eigenvectors of the normal Jacobian matrix in eq. (5) in direction $\vec{n}$ and are given by the columns of the matrix of right eigenvectors

$$
R_{pq}^{A_n} = \begin{pmatrix}
\lambda + 2\mu n_x^2 & -2\mu n_x n_y & n_y^2 & -2\mu n_x n_y & \lambda + 2\mu n_x^2 \\
\lambda + 2\mu n_y^2 & 2\mu n_x n_y & n_x^2 & 2\mu n_x n_y & \lambda + 2\mu n_y^2 \\
2\mu n_x n_y & \mu(n_x^2 - n_y^2) & -n_x n_y & \mu(n_x^2 - n_y^2) & 2\mu n_x n_y \\
n_x c_p & -n_y c_s & 0 & n_y c_s & -n_x c_p \\
n_y c_p & n_x c_s & 0 & -n_x c_s & -n_y c_p
\end{pmatrix}.
\tag{8}
$$

The derived eigenstructure of the elastic wave equations provides the necessary information to construct the ADER–DG scheme as described in the following Section 3.

3 THE NUMERICAL SCHEME

For the construction of the numerical scheme, we consider the general linear hyperbolic system of equations with variable coefficients as given in eq. (2). The computational domain $\Omega \in \mathbb{R}^2$ is divided in conforming triangular elements $\mathcal{T}^{(m)}$ being addressed by a unique index (m). Furthermore, we suppose the matrices A_{pq} and B_{pq} to be piecewise constant inside an element $\mathcal{T}^{(m)}$.

3.1 Semi-discrete Form of the Scheme

Inside each triangle $\mathcal{T}^{(m)}$ the solution of eq. (2) is approximated numerically by u_h using a linear combination of time-independent polynomial basis functions $\Phi_l(\xi, \eta)$ of degree N with support $\mathcal{T}^{(m)}$ and the time-dependent degrees of freedom $\hat{u}_{pl}^{(m)}(t)$:

$$
\left(u_h^{(m)}\right)_p (\xi, \eta, t) = \hat{u}_{pl}^{(m)}(t)\Phi_l(\xi, \eta).
\tag{9}
$$

ξ and η are the coordinates in a reference element $\mathcal{T}_E$ and are defined in eqs (17) and (18). The approximation space is denoted by V_h. We use orthogonal basis functions Φ_k that rely on the ideas originally developed by Dubiner (1991) and which are given, for example, in the book of Cockburn *et al.* (2000). Multiplying eq. (2) by a test function $\Phi_k \in V_h$ and integrating over a triangle $\mathcal{T}^{(m)}$ gives

$$
\int_{\mathcal{T}^{(m)}} \Phi_k \frac{\partial u_p}{\partial t} \, dV + \int_{\mathcal{T}^{(m)}} \Phi_k \left(A_{pq} \frac{\partial u_q}{\partial x} + B_{pq} \frac{\partial u_q}{\partial y} \right) dV = \int_{\mathcal{T}^{(m)}} \Phi_k S_p \, dV.
\tag{10}
$$

Integration of eq. (10) by parts then yields

$$
\int_{\mathcal{T}^{(m)}} \Phi_k \frac{\partial u_p}{\partial t} \, dV + \int_{\partial \mathcal{T}^{(m)}} \Phi_k F_p^h \, dS - \int_{\mathcal{T}^{(m)}} \left(\frac{\partial \Phi_k}{\partial x} A_{pq} u_q + \frac{\partial \Phi_k}{\partial y} B_{pq} u_q \right) dV = \int_{\mathcal{T}^{(m)}} \Phi_k S_p \, dV,
\tag{11}
$$

where a numerical flux F_p^h has been introduced in the surface integral since u_h may be discontinuous at an element boundary. As we suppose rotational invariance of the system in eq. (2) for the isotropic case, the flux can be derived for a coordinate system, which is aligned with the outward pointing unit normal vector $\vec{n} = (n_x, n_y)^T$ of an element boundary. The required transformation (rotation) of the unknowns in vector u_p from the global Cartesian system to the vector u_q^n in a local normal, that is, *edge-aligned*, coordinate system is given by

$$
u_p = T_{pq} u_q^n.
\tag{12}
$$

For the 2-D elastic wave equations the transformation matrix T_{pq} in eq. (12) reads as

$$
T_{pq} = \begin{pmatrix}
n_x^2 & n_y^2 & -2n_x n_y & 0 & 0 \\
n_y^2 & n_x^2 & 2n_x n_y & 0 & 0 \\
n_x n_y & -n_x n_y & n_x^2 - n_y^2 & 0 & 0 \\
0 & 0 & 0 & n_x & -n_y \\
0 & 0 & 0 & n_y & n_x
\end{pmatrix}.
\tag{13}
$$

For the system in eq. (2) we use the exact Riemann solver to compute the state at the element interfaces by upwinding. The flux is then computed with the Jacobian matrix in eq. (3), that is, with the material properties given in the considered element. In the global Cartesian xy-system the numerical flux F_p^h in eq. (11) for triangle $\mathcal{T}^{(m)}$ across the edge with one of the neighbour triangles $\mathcal{T}^{(m_j)}$, $j = 1, 2, 3$, is then given as

$$
F_p^h = \frac{1}{2} T_{pq} \left(A_{qr}^{(m)} + \left| A_{qr}^{(m)} \right| \right) (T_{rs})^{-1} \hat{u}_{sl}^{(m)} \Phi_l^{(m)}
$$
$$
+ \frac{1}{2} T_{pq} \left(A_{qr}^{(m)} - \left| A_{qr}^{(m)} \right| \right) (T_{rs})^{-1} \hat{u}_{sl}^{(m_j)} \Phi_l^{(m_j)},
\tag{14}
$$
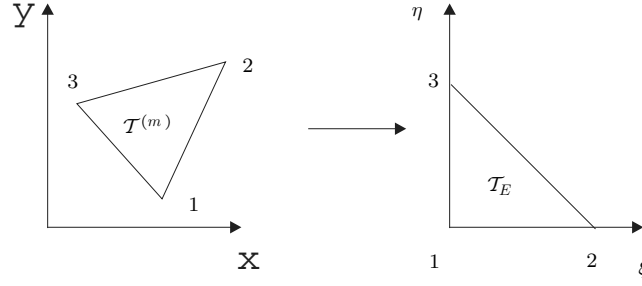
Figure 1. Transformation from the physical triangle $\mathcal{T}^{(m)}$ to the canonical reference triangle $\mathcal{T}_E$ with nodes (0,0), (1,0) and (0,1).

where $\hat{u}_{sl}^{(m)}\Phi_l^{(m)}$ and $\hat{u}_{sl}^{(m_j)}\Phi_l^{(m_j)}$ are the boundary extrapolated values of the numerical solution from element $\mathcal{T}^{(m)}$ and the jth side neighbour $\mathcal{T}^{(m_j)}$, respectively. The matrix $(T_{rs})^{-1}$ represents the back-transformation into the global xy-system. We point out that the boundary values of both elements adjacent to an interface contribute to the numerical flux. Furthermore, due to the rotation it is sufficient to evaluate the Jacobian matrix $A_{qr}^{(m)}$ in eq. (3) in x-direction with the material properties given in triangle $\mathcal{T}^{(m)}$. This way, the numerical flux respects the non-conservative form of the governing equation in (2). The notation $|A_{qr}^{(m)}|$ of the absolute value of the Jacobian matrix has the meaning of applying the absolute value operator to the eigenvalues given in eq. (6), that is,

$$\left|A_{qr}^{(m)}\right| = R_{pr}^A \left|\Lambda_{rs}\right| \left(R_{sq}^A\right)^{-1}, \quad \text{with} \quad |\Lambda_{rs}| = \mathrm{diag}\left(|s_1|, |s_2|, \ldots\right). \tag{15}$$

Now, inserting eqs (9) and (14) into eq. (11) and splitting the boundary integral into the contributions of each edge j of the triangle $\mathcal{T}^{(m)}$, we obtain

$$\frac{\partial}{\partial t}\hat{u}_{pl}^{(m)} \int_{\mathcal{T}^{(m)}} \Phi_k \Phi_l \, dV$$

$$+ \sum_{j=1}^{3} T_{pq}^j \frac{1}{2}\left(A_{qr}^{(m)} + \left|A_{qr}^{(m)}\right|\right)(T_{rs}^j)^{-1}\hat{u}_{sl}^{(m)} \int_{(\partial\mathcal{T}^{(m)})_j} \Phi_k^{(m)}\Phi_l^{(m)} \, dS$$

$$+ \sum_{j=1}^{3} T_{pq}^j \frac{1}{2}\left(A_{qr}^{(m)} - \left|A_{qr}^{(m)}\right|\right)(T_{rs}^j)^{-1}\hat{u}_{sl}^{(m_j)} \int_{(\partial\mathcal{T}^{(m)})_j} \Phi_k^{(m)}\Phi_l^{(m_j)} \, dS$$

$$- A_{pq}\hat{u}_{ql}^{(m)} \int_{\mathcal{T}^{(m)}} \frac{\partial\Phi_k}{\partial x}\Phi_l \, dV - B_{pq}\hat{u}_{ql}^{(m)} \int_{\mathcal{T}^{(m)}} \frac{\partial\Phi_k}{\partial y}\Phi_l \, dV = \int_{\mathcal{T}^{(m)}} \Phi_k S_p \, dV. \tag{16}$$

Eq. (16) is written in the global xy-system. If we transform each physical triangle $\mathcal{T}^{(m)}$ to a canonical reference triangle $\mathcal{T}_E$ in a $\xi\eta$-reference system as shown in Fig. 1, the method can be implemented much more efficiently since many integrals can be pre-computed beforehand in this reference system. The coordinate transformation is defined by

$$x = x_1 + (x_2 - x_1)\xi + (x_3 - x_1)\eta,$$
$$y = y_1 + (y_2 - y_1)\xi + (y_3 - y_1)\eta, \tag{17}$$

with the inverse transformation

$$\xi = \frac{1}{|J|}((x_3 y_1 - x_1 y_3) + x(y_3 - y_1) + y(x_1 - x_3)),$$
$$\eta = \frac{1}{|J|}((x_1 y_2 - x_2 y_1) + x(y_1 - y_2) + y(x_2 - x_1)), \tag{18}$$

where $|J| = (x_2 - x_1)(y_3 - y_1) - (x_3 - x_1)(y_2 - y_1)$ is the determinant of the Jacobian matrix of the transformation being equal to twice the triangle's surface.

With respect to the transformation, we have furthermore

$$dx\,dy = |J|d\xi\,d\eta, \tag{19}$$

and the transformed gradients

$$\begin{pmatrix} \frac{\partial}{\partial x} \\ \frac{\partial}{\partial y} \end{pmatrix} = \begin{pmatrix} \frac{\partial\xi}{\partial x} & \frac{\partial\eta}{\partial x} \\ \frac{\partial\xi}{\partial y} & \frac{\partial\eta}{\partial y} \end{pmatrix} \begin{pmatrix} \frac{\partial}{\partial\xi} \\ \frac{\partial}{\partial\eta} \end{pmatrix}. \tag{20}$$

Integrating in the reference system using eqs (19) and (20), the semi-discrete DG formulation of eq. (16) reads as

$$\frac{\partial}{\partial t}\hat{u}_{pl}^{(m)}\,|J|\int_{\mathcal{T}_E}\Phi_k\Phi_l\,d\xi\,d\eta$$

$$+\sum_{j=1}^{3}T_{pq}^{j}\frac{1}{2}\left(A_{qr}^{(m)}+\left|A_{qr}^{(m)}\right|\right)\left(T_{rs}^{j}\right)^{-1}\hat{u}_{sl}^{(m)}|S_j|\int_{0}^{1}\Phi_k^{(m)}(\chi_j)\Phi_l^{(m)}(\chi_j)d\chi_j$$

$$+\sum_{j=1}^{3}T_{pq}^{j}\frac{1}{2}\left(A_{qr}^{(m)}-\left|A_{qr}^{(m)}\right|\right)\left(T_{rs}^{j}\right)^{-1}\hat{u}_{sl}^{(m_j)}|S_j|\int_{0}^{1}\Phi_k^{(m)}(\chi_j)\Phi_l^{(m_j)}(\chi_j)d\chi_j$$

$$-A_{pq}^{*}\hat{u}_{ql}^{(m)}\,|J|\int_{\mathcal{T}_E}\frac{\partial\Phi_k}{\partial\xi}\Phi_l\,d\xi\,d\eta-B_{pq}^{*}\hat{u}_{ql}^{(m)}\,|J|\int_{\mathcal{T}_E}\frac{\partial\Phi_k}{\partial\eta}\Phi_l\,d\xi\,d\eta=|J|\int_{\mathcal{T}_E}\Phi_k S_p\,d\xi\,d\eta\ ,\tag{21}$$

with the special linear combination of the Jacobians

$$A_{pq}^{*}=A_{pq}\frac{\partial\xi}{\partial x}+B_{pq}\frac{\partial\xi}{\partial y},\tag{22}$$

$$B_{pq}^{*}=A_{pq}\frac{\partial\eta}{\partial x}+B_{pq}\frac{\partial\eta}{\partial y}.\tag{23}$$

In eq. (21) the variable $0\le\chi_j\le1$ is introduced to parametrize the jth edge of the reference triangle and $|S_j|$ is the length of this edge in physical space. The following integrals

$$M_{kl}=\int_{\mathcal{T}_E}\Phi_k\Phi_l\,d\xi\,d\eta,\tag{24}$$

$$F_{kl}^{j,0}=\int_{0}^{1}\Phi_k^{(m)}(\chi_j)\Phi_l^{(m)}(\chi_j)\,d\chi_j,\tag{25}$$

$$F_{kl}^{j,i}=\int_{0}^{1}\Phi_k^{(m)}(\chi_j)\Phi_l^{(m_j)}(\chi_j)\,d\chi_j,\tag{26}$$

$$K_{kl}^{\xi}=\int_{\mathcal{T}_E}\frac{\partial\Phi_k}{\partial\xi}\Phi_l\,d\xi\,d\eta,\tag{27}$$

$$K_{kl}^{\eta}=\int_{\mathcal{T}_E}\frac{\partial\Phi_k}{\partial\eta}\Phi_l\,d\xi\,d\eta,\tag{28}$$

can all be calculated beforehand by a computer algebra system (e.g. Maple). On an unstructured mesh the flux matrices $F_{kl}^{j,0}$ account for the contribution of the element $\mathcal{T}^{(m)}$ itself to the fluxes over all three edges j and the flux matrices $F_{kl}^{j,i}$ account for the contribution of the elements' direct side neighbours $\mathcal{T}^{(m_j)}$ to the fluxes over the edges j. Index $1\le i\le3$ indicates the local number of the common edge in neighbour $\mathcal{T}^{(m_j)}$ and depends on the mesh generator. Matrices K_{kl}^{ξ} and K_{kl}^{η} are analogous to the stiffness matrices of classical continuous FE. We emphasize that for the DG method as given by eq. (21) *no* assembly of global mass-, flux- and stiffness matrices is needed in contrast to continuous FE schemes. The method is completely local and, therefore, well suited for parallelization. Hence, there are no large global linear equation systems to solve and due to the choice of orthogonal basis functions the inversion of the diagonal DG mass matrix M_{kl} is trivial. Examples for matrices (24)–(28) can be found in (Dumbser & Munz 2005b). On a given mesh, where index i is known, only three of the nine possible matrices $F_{kl}^{j,i}$ are used per element.

If the semi-discrete eq. (21) is integrated in time with a Runge-Kutta method, we obtain the quadrature-free Runge-Kutta DG approach developed by Atkins & Shu (1998).

3.2 The ADER time discretization

The efficiency of Runge-Kutta time discretization schemes drastically decreases if the order of accuracy becomes greater than four due to the so-called Butcher barriers (Butcher 1987), which cause the number of intermediate stages to become larger than the formal order of accuracy. Therefore, we apply the ADER approach of Toro *et al.* (2001) to the semi-discrete form of the DG scheme (eq. 21) in order to achieve an arbitrarily accurate time discretization.

The main ingredients of the ADER approach (Toro & Titarev 2002) are a Taylor expansion in time, the solution of derivative Riemann problems to approximate the space derivatives at the interface and the Cauchy-Kovalewski procedure for replacing the time derivatives in the Taylor series by space derivatives. In this Section we show how the ADER approach can be used for high-order time integration of the DG method for linear hyperbolic systems with external source terms and denote the proposed scheme ADER–DG.

For the development of linear ADER–DG schemes, we first need a general formula for the Cauchy-Kovalewski procedure in order to replace the kth time derivative by pure space derivatives. Since all our basis functions are given in the $\xi\eta$-system, we need a Cauchy-Kovalewski procedure, which makes use of the spatial derivatives with respect to ξ and η. Therefore, we rewrite our original PDE (2) with the use of

eq. (20) as

$$\frac{\partial u_p}{\partial t} + A_{pq}\left(\frac{\partial u_q}{\partial \xi}\frac{\partial \xi}{\partial x} + \frac{\partial u_q}{\partial \eta}\frac{\partial \eta}{\partial x}\right) + B_{pq}\left(\frac{\partial u_q}{\partial \xi}\frac{\partial \xi}{\partial y} + \frac{\partial u_q}{\partial \eta}\frac{\partial \eta}{\partial y}\right) = S_p, \tag{29}$$

rearrange this equation to get

$$\frac{\partial u_p}{\partial t} + \left(A_{pq}\frac{\partial \xi}{\partial x} + B_{pq}\frac{\partial \xi}{\partial y}\right)\frac{\partial u_q}{\partial \xi} + \left(A_{pq}\frac{\partial \eta}{\partial x} + B_{pq}\frac{\partial \eta}{\partial y}\right)\frac{\partial u_q}{\partial \eta} = S_p, \tag{30}$$

and finally, by using the definitions in eqs (22) and (23), we obtain

$$\frac{\partial u_p}{\partial t} + A^*_{pq}\frac{\partial u_q}{\partial \xi} + B^*_{pq}\frac{\partial u_q}{\partial \eta} = S_p. \tag{31}$$

The kth time derivative as a function of pure space derivatives in the $\xi\eta$-reference system is the result of the Cauchy-Kovalewski procedure applied to eq. (31) and is given by

$$\frac{\partial^k}{\partial t^k}u_p = (-1)^k\left(A^*_{pq}\frac{\partial}{\partial \xi} + B^*_{pq}\frac{\partial}{\partial \eta}\right)^k u_q + \sum_{s=0}^{k-1}(-1)^s\left(A^*_{pq}\frac{\partial}{\partial \xi} + B^*_{pq}\frac{\partial}{\partial \eta}\right)^s \frac{\partial^{k-s-1}}{\partial t^{k-s-1}}S_q. \tag{32}$$

Proof.

We proof eq. (32) by complete induction. For $k = 0$ it is trivially fulfilled, so we start with $k = 1$:

$$\frac{\partial}{\partial t}u_p = (-1)\left(A^*_{pq}\frac{\partial}{\partial \xi} + B^*_{pq}\frac{\partial}{\partial \eta}\right)u_q + S_p. \tag{33}$$

Eq. (33) is nothing else than eq. (31) rewritten in a different form, so for $k = 1$ formula (32) holds. If we now suppose that it holds for k, one can easily proof that from this assumption it will also hold for $k + 1$. Deriving eq. (32) with respect to time yields

$$\frac{\partial^{k+1}}{\partial t^{k+1}}u_p = (-1)^k\left(A^*_{pq}\frac{\partial}{\partial \xi} + B^*_{pq}\frac{\partial}{\partial \eta}\right)^k \frac{\partial}{\partial t}u_q + \sum_{s=0}^{k-1}(-1)^s\left(A^*_{pq}\frac{\partial}{\partial \xi} + B^*_{pq}\frac{\partial}{\partial \eta}\right)^s \frac{\partial^{k-s}}{\partial t^{k-s}}S_q, \tag{34}$$

which by using eq. (33) becomes

$$\frac{\partial^{k+1}}{\partial t^{k+1}}u_p = (-1)^k\left(A^*_{pq}\frac{\partial}{\partial \xi} + B^*_{pq}\frac{\partial}{\partial \eta}\right)^k \left((-1)\left(A^*_{qr}\frac{\partial}{\partial \xi} + B^*_{qr}\frac{\partial}{\partial \eta}\right)u_r + S_q\right) + \sum_{s=0}^{k-1}(-1)^s\left(A^*_{pq}\frac{\partial}{\partial \xi} + B^*_{pq}\frac{\partial}{\partial \eta}\right)^s \frac{\partial^{k-s}}{\partial t^{k-s}}S_q.$$

Rearranging terms yields

$$\frac{\partial^{k+1}}{\partial t^{k+1}}u_p = (-1)^{k+1}\left(A^*_{pq}\frac{\partial}{\partial \xi} + B^*_{pq}\frac{\partial}{\partial \eta}\right)^{k+1}u_q + (-1)^k\left(A^*_{pq}\frac{\partial}{\partial \xi} + B^*_{pq}\frac{\partial}{\partial \eta}\right)^k S_q$$
$$+ \sum_{s=0}^{k-1}(-1)^s\left(A^*_{pq}\frac{\partial}{\partial \xi} + B^*_{pq}\frac{\partial}{\partial \eta}\right)^s \frac{\partial^{k-s}}{\partial t^{k-s}}S_q,$$

and finally

$$\frac{\partial^{k+1}}{\partial t^{k+1}}u_p = (-1)^{k+1}\left(A^*_{pq}\frac{\partial}{\partial \xi} + B^*_{pq}\frac{\partial}{\partial \eta}\right)^{k+1}u_q + \sum_{s=0}^{k}(-1)^s\left(A^*_{pq}\frac{\partial}{\partial \xi} + B^*_{pq}\frac{\partial}{\partial \eta}\right)^s \frac{\partial^{k-s}}{\partial t^{k-s}}S_q. \tag{35}$$

In order to be able to perform many computations in the reference element $\mathcal{T}_E$, we represent the source-terms S_p in a space-time basis over the space–time element $\mathcal{T}_E \times [t^n; t^{n+1}]$, where $\Delta t = t^{n+1} - t^n$ denotes the time step. The basis is constructed via tensor product of the spatial basis functions $\Phi_m(\xi, \eta)$ used already in eq. (9) and some new temporal basis functions $\Psi_l(t)$ for which we choose classical Legendre polynomials in the interval of one time step $[t^n; t^{n+1}]$:

$$S_p(\xi, \eta, t) = \hat{S}_{plm}\Psi_l(t)\Phi_m(\xi, \eta). \tag{36}$$

Given the source term $S_p(\xi, \eta, t)$ by some analytic function or from discrete measurement data, we first perform L^2 projection in order to compute the unknown coefficients $\hat{S}_{plm}$ in eq. (36). In the following, $\langle ., . \rangle_{(\cdot)}$ denotes the inner product over the domain $(\cdot)$.

$$\langle S_p(\xi, \eta, t), \Psi_j\Phi_k\rangle_{\mathcal{T}_E \times [t^n; t^{n+1}]} = \hat{S}_{plm}\langle \Psi_j\Phi_k, \Phi_m\Psi_l\rangle_{\mathcal{T}_E \times [t^n; t^{n+1}]}. \tag{37}$$

Since spatial and temporal integration are independent due to the tensor product formulation, we get

$$\langle S_p(\xi, \eta, t), \Psi_j\Phi_k\rangle_{\mathcal{T}_E \times [t^n; t^{n+1}]} = \hat{S}_{plm}\langle \Psi_j, \Psi_l\rangle_{[t^n; t^{n+1}]}\langle \Phi_m, \Phi_k\rangle_{\mathcal{T}_E}. \tag{38}$$

Due to the orthogonality of the basis functions, the appearing mass matrices are diagonal and can be trivially inverted.

We point out that it is a key issue to use the Cauchy-Kovalewski procedure in the form (32) since it allows us to pre-calculate many matrices beforehand, as we will see in the following.

We develop the solution of eq. (2) in a Taylor series in time up to order N,

$$u_p(\xi, \eta, t) = \sum_{k=0}^{N}\frac{t^k}{k!}\frac{\partial^k}{\partial t^k}u_p(\xi, \eta, 0), \tag{39}$$

and replace time derivatives by space derivatives, using eqs (9), (32) and (36):

$$u_p(\xi, \eta, t) = \sum_{k=0}^{N} \frac{t^k}{k!} (-1)^k \left(A_{pq}^* \frac{\partial}{\partial \xi} + B_{pq}^* \frac{\partial}{\partial \eta} \right)^k \Phi_l \hat{u}_{ql}(0)$$

$$+ \sum_{s=0}^{k-1} (-1)^s \left(A_{pq}^* \frac{\partial}{\partial \xi} + B_{pq}^* \frac{\partial}{\partial \eta} \right)^s \frac{\partial^{k-s-1}}{\partial t^{k-s-1}} \Psi_l(t) \Phi_m(\xi, \eta) \hat{S}_{qlm}.$$

This approximation can now be projected onto each basis function in order to get an approximation of the evolution of the degrees of freedom during one time step from time level n to time level $n + 1$. We obtain

$$\int_0^{\Delta t} \hat{u}_{pl}(\tau) \, d\tau = I_{plqm}(\Delta t) \hat{u}_{qm}(0) + I_{plqom}^S(\Delta t) \hat{S}_{qom}, \tag{40}$$

with

$$I_{plqm}(\Delta t) = \frac{\left\langle \Phi_n, \sum_{k=0}^{N} \frac{\Delta t^{(k+1)}}{(k+1)!} (-1)^k \left(A_{pq}^* \frac{\partial}{\partial \xi} + B_{pq}^* \frac{\partial}{\partial \eta} \right)^k \Phi_m(\xi) \right\rangle_{\mathcal{T}_E}}{\langle \Phi_n, \Phi_l \rangle_{\mathcal{T}_E}}, \tag{41}$$

and an additional tensor taking into account the source term during time integration,

$$I_{plqom}^S(\Delta t) = \frac{\left\langle \Phi_n, \sum_{k=0}^{N} \frac{\Delta t^{(k+1)}}{(k+1)!} \sum_{s=0}^{k-1} (-1)^s \left(A_{pq}^* \frac{\partial}{\partial \xi} + B_{pq}^* \frac{\partial}{\partial \eta} \right)^s \Phi_m \frac{\partial^{k-s-1}}{\partial t^{k-s-1}} \Psi_o \right\rangle_{\mathcal{T}_E}}{\langle \Phi_n, \Phi_l \rangle_{\mathcal{T}_E}}. \tag{42}$$

To simplify notation we skip the index$^{(m)}$ for the two tensors given in eqs (41) and (42) but remark that they may vary from one element to another depending on the variation of the material and, therefore, of the Jacobian matrices A_{pq}^* and B_{pq}^*.

With those definitions we finally obtain the fully discrete ADER–DG scheme

$$\left[\left(\hat{u}_{pl}^{(m)} \right)^{n+1} - \left(\hat{u}_{pl}^{(m)} \right)^n \right] |J| M_{kl}$$

$$+ \frac{1}{2} \sum_{j=1}^{3} T_{pq}^j \left(A_{qr}^{(m)} + \left| A_{qr}^{(m)} \right| \right) (T_{rs}^j)^{-1} |S_j| F_{kl}^{j,0} \cdot \left(I_{slmn}(\Delta t) \left(\hat{u}_{mn}^{(m)} \right)^n + I_{slmon}^S(\Delta t) \left(\hat{S}_{mon}^{(m)} \right)^n \right)$$

$$+ \frac{1}{2} \sum_{j=1}^{3} T_{pq}^j \left(A_{qr}^{(m)} + \left| A_{qr}^{(m)} \right| \right) (T_{rs}^j)^{-1} |S_j| F_{kl}^{j,i} \cdot \left(I_{slmn}(\Delta t) \left(\hat{u}_{mn}^{(m_j)} \right)^n + I_{slmon}^S(\Delta t) \left(\hat{S}_{mon}^{(m_j)} \right)^n \right)$$

$$- |J| \left(A_{pq}^* K_{kl}^\xi + B_{pq}^* K_{kl}^\eta \right) \cdot \left(I_{slmn}(\Delta t) \left(\hat{u}_{mn}^{(m)} \right)^n + I_{slmon}^S(\Delta t) \left(\hat{S}_{mon}^{(m)} \right)^n \right)$$

$$- \int_{t^n}^{t^{n+1}} |J| \int_{\mathcal{T}_E} \Phi_k S_p \, d\xi \, d\eta \, dt = M_{kl} |J| \cdot \int_{t^n}^{t^{n+1}} \Psi_o(t) \, d\tau \cdot \hat{S}_{pol}^{(m)}. \tag{43}$$

On rectangular elements, the scheme takes the same form except that one has to consider the contribution of four edges instead of three in the case of triangles. The eqs (17) and (18) of the transformation remain unchanged, see (Schwarz 1988). The scheme is quadrature-free and performs high-order time integration from t^n to t^{n+1} in one single step. It thus needs the same memory as a first-order explicit Euler time-stepping scheme. Note that for any DG scheme the initial condition at t^0 must be projected onto the degrees of freedom via L^2 projection.

3.3 Point sources

In the previous subsection we described the discretization of source terms that are continuous in space and time. However, many geophysical applications as well as classical test cases with analytical solutions, such as, for example, Lamb's problem require point sources that are characterized by a Dirac Delta distribution in space and a so-called source time function $S_p^T(t)$. Within the ADER–DG framework, it is straightforward to include such point sources at *arbitrary* positions in the computational domain. It is *not* necessary that the Delta distributions coincide with a mesh point since the arising integrals can always be evaluated analytically using the properties of the Delta distribution. The source terms considered here thus have the form

$$S_p(x, y, t) = S_p^T(t) \cdot \delta(\vec{x} - \vec{x}_s), \tag{44}$$

where $\delta(\vec{x})$ denotes the usual Dirac Delta distribution with its well-known properties. Since the source term is given by the Delta distribution in space, we only have to express the time-dependent part, that is, the source time function $S_p^T(t)$, via some temporal basis functions similar to eq. (9), which leads to a discrete representation of a point source given by

$$S_p(x, y, t) = \hat{S}_{pl} \Psi_l(t) \cdot \delta(\vec{x} - \vec{x}_s). \tag{45}$$

Similar to eq. (40) we obtain the following expression that can be directly inserted on the left-hand side of eq. (43),

$$\int_0^{\Delta t} \hat{u}_{pl}(\tau) \, d\tau = I_{plqm}(\Delta t) \hat{u}_{qm}(0) + I_{plqm}^S(\Delta t) \hat{S}_{qm}, \tag{46}$$

with $I_{plqm}(\Delta t)$ still given by eq. (41) and a correction term $I^S_{plqm}(\Delta t)$ due to the point source given by

$$I^S_{plqm}(\Delta t) = \frac{\sum_{k=0}^{N} \frac{\Delta t^{(k+1)}}{(k+1)!} \sum_{s=0}^{k-1} \left(A^*_{pq} \frac{\partial}{\partial \xi} + B^*_{pq} \frac{\partial}{\partial \eta} \right)^s \Phi_n \left(\vec{\xi}_s \right) \cdot \frac{\partial^{k-s-1}}{\partial t^{k-s-1}} \Psi_m}{|J| \langle \Phi_n, \Phi_l \rangle_{\mathcal{T}_E}}. \tag{47}$$

if the point source is located inside the corresponding element, that is, $\vec{x}_s \in \mathcal{T}^{(m)}$, or zero elsewhere. Note that $\vec{\xi}_s$ is the location of the point source in the reference element. Eq. (47) follows directly from eq. (42) using the properties of the Delta distribution and its derivatives. The right-hand side of eq. (43) reduces to zero except of those elements that contain a point sources, where it then becomes

$$\int_{t^n}^{t^{n+1}} |J| \int_{\mathcal{T}^E} \Phi_k S_p \, d\xi \, d\eta \, dt = \Phi_k(\vec{\xi}_s) \cdot \int_{t^n}^{t^{n+1}} S_p^T(t) \, dt. \tag{48}$$

Since the test functions are evaluated exactly at the source position $\vec{x}_s$ in a triangle $\mathcal{T}^{(m)}$, that is, at $\vec{\xi}_s$ in the reference triangle $\mathcal{T}_E$, the point sources may be located at *any* position inside the computational domain. If the point $\vec{x}_s$ coincides with a mesh point or element edge, only one of the adjacent elements is allowed to contain the source. This choice, however, is arbitrary.

3.4 An efficient algorithm for the Cauchy-Kovalewski procedure of linear systems

On unstructured meshes, we must evaluate eq. (41) in each triangle in each time step, if we do not want to store all the tensor coefficients $I_{plqm}(\Delta t)$ for each triangle. Therefore, in the following we show a very efficient algorithm for its evaluation on the reference element. Eq. (41) contains a binomial formula for matrices whose products unfortunately do not commute in the general case. If expanded explicitly, eq. (41) becomes

$$I_{plqm}(\Delta t) = \langle \Phi_n, \Phi_l \rangle^{-1} \left\langle \Phi_n, \sum_{k=0}^{N} \frac{\Delta t^{(k+1)}}{(k+1)!} (-1)^k \sum_{n_B=0}^{k} S_{pq} \left(A^*_{pq}, B^*_{pq}, k - n_B, n_B \right) \frac{\partial^k}{\partial \xi^{(k-n_B)} \partial \eta^{n_B}} \Phi_m \right\rangle. \tag{49}$$

Hence, in the evaluation of eq. (41) we have to compute the sums S_{pq} of all products of A^*_{pq} and B^*_{pq} in which matrix A^*_{pq} appears $n_A = k - n_B$ times and matrix B^*_{pq} appears n_B times, taking into account all possible matrix permutations. Without proof, we give a recursive algorithm defining the S_{pq} in step 1 of the following Algorithm. It recycles all previously computed data if implemented in an unrolled manner, storing intermediate results. In the Algorithm, δ_{pq} denotes the usual Kronecker symbol.

Algorithm: (efficient Cauchy-Kovalewski procedure)

Step 1: Compute and store temporarily the sums of all matrix products of A^*_{pq} and B^*_{pq} with all possible permutations,

$$S_{pq}\left(A^*_{pq}, B^*_{pq}, n_A, n_B \right) := 0, \qquad \text{if} \qquad n_A < 0 \quad \vee \quad n_B < 0,$$

$$S_{pq}\left(A^*_{pq}, B^*_{pq}, 0, 0 \right) \quad := \delta_{pq},$$

$$S_{pq}\left(A^*_{pq}, B^*_{pq}, n_A, n_B \right) = S_{pr}\left(A^*_{pr}, B^*_{pr}, n_A - 1, n_B \right) \cdot A^*_{rq} +$$
$$S_{pr}\left(A^*_{pr}, B^*_{pr}, n_A, n_B - 1 \right) \cdot B^*_{rq},$$

$$\forall \quad 0 \le n_A + n_B \le N.$$

Step 2: Exchange summation and integration in eq. (49) and compute $I_{plqm}(\Delta t)$ as:

$$I_{plqm}(\Delta t) = \sum_{k=0}^{N} \frac{\Delta t^{(k+1)}}{(k+1)!} (-1)^k \sum_{n_B=0}^{k} S_{pq} \left(A^*_{pq}, B^*_{pq}, k - n_B, n_B \right) \langle \Phi_n, \Phi_l \rangle^{-1} \left\langle \Phi_n, \frac{\partial^k}{\partial \xi^{(k-n_B)} \partial \eta^{n_B}} \Phi_m \right\rangle.$$

In the presence of source terms, we need to compute the additional tensor of eq. (42) as:

$$I^S_{plqom}(\Delta t) = \sum_{k=0}^{N} \frac{\Delta t^{(k+1)}}{(k+1)!} \sum_{s=0}^{k-1} (-1)^s \sum_{n_B=0}^{s} S_{pq} \left(A^*_{pq}, B^*_{pq}, s - n_B, n_B \right) \langle \Phi_n, \Phi_l \rangle^{-1} \left\langle \Phi_n, \frac{\partial^k}{\partial \xi^{(k-n_B)} \partial \eta^{n_B}} \Phi_m \right\rangle \frac{\partial^{k-s-1}}{\partial t^{k-s-1}} \Psi_o.$$

This algorithm is used in each triangle $\mathcal{T}^{(m)}$ in each time step. However, all projections of the space derivatives of the basis functions Φ onto all the test functions, as they appear in step 2 of the Algorithm, can be pre-computed once and then stored. They are defined on the canonical reference triangle and depend neither on the mesh nor on the time step. Similarly, all time derivatives of the basis functions Ψ can be pre-computed for a canonical reference interval in time.

4 BOUNDARY CONDITIONS

There is a variety of physically meaningful boundary conditions of an elastic medium. However, the two important types of boundaries are *absorbing* and *free surface* boundaries.

4.1 Absorbing boundaries

At absorbing boundaries, no waves are supposed to enter the computational domain and those waves that are travelling out should be able to pass the boundary without reflections. There is a whole scientific community dealing with absorbing or non-reflective boundary conditions, however, in this Section we present only a very simple approach that so far yielded satisfactory results, at least for our purposes. The numerical flux (eq. 14) is based on the solution of the Riemann-Problem given by the jump across the element interface. It is a strict upwind method, that is, outgoing waves at an element interface are only influenced by the state in the element itself and not by the state in the neighbour. In contrast, the flux contribution of incoming waves is purely due to the state in the neighbour element. Thus, a very simple implementation of absorbing boundary conditions is to use the following numerical flux in eq. (43) at all those edges that coincide with an absorbing boundary:

$$F_p^{\text{AbsorbBC}} = \frac{1}{2} T_{pq} \left(A_{qr}^{(m)} + \left| A_{qr}^{(m)} \right| \right) (T_{rs})^{-1} \hat{u}_{sl}^{(m)} \Phi_l^{(m)}. \tag{50}$$

The flux function (50) allows only for outgoing waves, which are merely defined by the state in the element due to upwinding. Since incoming waves are not allowed, the respective flux contribution must vanish. We are aware that these absorbing boundary conditions have some problems at corners or for *grazing* incidence of waves. Therefore, in future work, approaches like the perfectly matched layer technique, as introduced in (Bérenger 1994) and applied in (Collino & Tsogka 2001; Komatitsch & Tromp 2003) should be incorporated to improve the performance of the proposed scheme for such boundaries.

4.2 Free surface boundaries

On the free surface of an elastic medium, the normal stress and the shear stresses with respect to the boundary are determined by physical constraints. Outside the elastic medium, there are no external forces that retract the particles into their original position. Therefore, the normal stress and the shear stress values at the free surface have to be zero. In contrast to classical continuous FE methods or SEM we have no direct control on the values at the boundaries within the DG framework. However, the boundary conditions can be imposed via the numerical flux, as in the FV framework. Considering that the numerical flux is based on the solution of a Riemann problem at an element interface and given some boundary extrapolated values from inside the computational domain on a free surface, we must solve a so-called inverse Riemann problem such that its solution yields exactly the free surface boundary conditions *at* the domain boundary. In the particular case of the free surface, the solution of the inverse Riemann problem can be obtained via symmetry considerations. For those components of the state vector u_p that we want to be zero at the domain boundary, we prescribe a virtual boundary extrapolated component on the outside of the interface that has the same magnitude but opposite sign. For the other components we just copy the inside values to the outside. For the free surface boundary condition the resulting numerical flux function in eq. (43) can then be formulated as follows,

$$F_p^{\text{FreeBC}} = \frac{1}{2} T_{pq} \left(A_{qr}^{(m)} + \left| A_{qr}^{(m)} \right| \right) (T_{rs})^{-1} \hat{u}_{sl}^{(m)} \Phi_l^{(m)} +$$
$$+ \frac{1}{2} T_{pq} \left(A_{qr}^{(m)} - \left| A_{qr}^{(m)} \right| \right) \Gamma_{rs} (T_{st})^{-1} \hat{u}_{tl}^{(m)} \Phi_l^{(m)}, \tag{51}$$

where the matrix $\Gamma_{rs} = \text{diag} \left(-1, 1, -1, 1, 1 \right)$ accounts for the mirroring of normal and shear stresses. We remark that the solution of the inverse Riemann-Problem is *not* equivalent to the FD approach of adding fictitious *ghost* points, but is similar to the FV framework and provides the exact values of the normal and shear stresses as required by the free surface boundary condition. Numerical examples in Section 6 confirm the performance and accuracy of this approach.

5 CONVERGENCE STUDY

In this Section we numerically determine the convergence orders of the proposed ADER–DG schemes first without source term and secondly with continuous source terms.

5.1 Convergence without source

As test case we solve the 2-D homogeneous elastic wave equations in (1) with $S_p = 0$, $p = 1, \ldots, 5$, on a square shaped domain $\Omega = [-50, 50] \times [-50, 50] \in \mathbb{R}^2$ with four periodic boundaries. We consider the initial condition

$$u_p^0 = u_p(\vec{x}, 0) = R_{p2}^{A_n} \sin(\vec{k} \cdot \vec{x}) + R_{p5}^{A_n} \sin(\vec{k} \cdot \vec{x}), \tag{52}$$
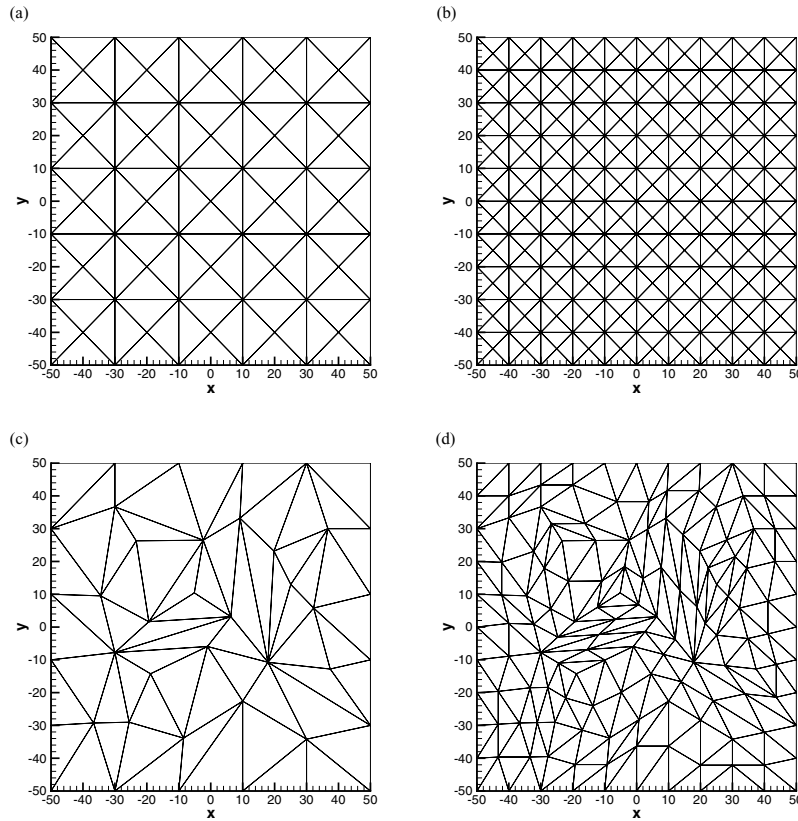
with the wavenumber

$$\vec{k} = (k_x, k_y)^T = \frac{2\pi}{25} (1, 1)^T. \tag{53}$$

The vectors $R_{p2}^{A_n}$ and $R_{p5}^{A_n}$ are two of the eigenvectors in eq. (8). Therefore, the initial condition in eq. (52) creates a plane sinusoidal P wave travelling along the diagonal direction $\vec{n} = (1, 1)^T$, as well as a plane sinusoidal S wave travelling into the opposite direction.

The homogeneous material parameters are set to

$$\lambda = 2, \qquad \mu = 1, \qquad \rho = 1, \tag{54}$$

Figure 2. Meshes for the analysis of the numerical convergence orders: (a) regular mesh, (b) refined regular mesh (c) irregular mesh, (d) refined irregular mesh.

throughout the computational domain Ω leading to the constant wave propagation velocities

$$c_p = 2, \qquad c_s = 1, \tag{55}$$

for the P and S wave, respectively. The total simulation time T is set to $T = 100\sqrt{2}$, such that the P and S waves at simulation time $t = T$ coincide with the initial condition at time $t = 0$. Therefore, the exact reference solution is given by the initial condition in eq. (52), that is,

$$u_p(\vec{x}, T) = u_p(\vec{x}, 0). \tag{56}$$

The stability of our explicit time-stepping scheme is controlled by the CFL number, introduced by Courant, Courant *et al.* (1928). In all computations the CFL number is set to 50 per cent of the stability limit $\frac{1}{2N+1}$ of Runge-Kutta DG schemes. For a thorough investigation of the linear stability properties of the ADER–DG schemes via a von Neumann analysis see (Dumbser 2005).

The numerical experiments to determine the convergence orders are performed on two sequences of regular and irregular triangular meshes. Each sequence consists of four meshes with decreasing mesh width. The first two meshes of each sequence are shown in Fig. 2.

For the regular mesh the refinement is simply controlled by changing the number of mesh elements in each dimension. For the irregular meshes we use the so-called *red-refinement*, where each triangle is refined subsequently by dividing it into four similar subtriangles, see (Hempel 1995; Meister & Struckmeier 2002) for details or Figs 2(c) and (d). We characterize the refinement state of a mesh by the maximum diameter h of the circumscribed circles of all triangular elements.

In Tables 1 and 2 the errors in L^∞ and L^2 norm of the normal stress σ_{xx} are given in relation to h for the regular and irregular meshes. The corresponding numerical convergence orders $\mathcal{O}_{L^\infty}$ and $\mathcal{O}_{L^2}$ are determined by two successively refined meshes. Furthermore, we present the total number N_d of degrees of freedom, which is a measure of required storage space during runtime. Besides we list the number of iterations I necessary to reach the final simulation time T. The computations were carried out on a Pentium Xeon 3.6 GHz processor with 4GB of RAM and the obtained CPU times in seconds are also listed in Tables 1 and 2.

Based on these convergence results, we state that the proposed ADER–DG schemes achieve the expected convergence orders on both regular and irregular meshes. We note that the ADER–DG $\mathcal{O}10$ schemes for the finest meshes in both cases, regular and irregular, seem to reach machine precision. Therefore, the convergence orders slightly drop below the expected values. Also we mention that the CPU time to reach the final simulation time $t = T$ is much larger for the irregular meshes. This is due to the small time steps caused by the CFL condition of the smallest diameter of the inscribed circle of all triangles (see Figs 2c and d).

A visual comparison of our results with results of a second-order FD scheme and SEM of order 7, that is, using P6 elements, is given in Figs 3 and 4. We plot the errors in L^∞ norm against mesh spacing h, total number of degrees of freedom N_d, and CPU time. The results of the SEM are obtained by the 2-D-SEM code provided by Bernhard Schubert (Department of Geophysics, Ludwig-Maximilians-University,

Table 1. Convergence rates of σ_{xx} from order 2 to 10 of ADER–DG on regular meshes.

h	L^∞	$\mathcal{O}_{L^\infty}$	L^2	$\mathcal{O}_{L^2}$	N_d	I	CPU [s]
2.108	1.542×10^0	–	1.044×10^2	–	7500	1305	123
1.054	4.087×10^{-1}	1.916	2.760×10^1	1.919	30 000	2575	892
0.703	1.769×10^{-1}	2.065	1.202×10^1	2.051	67 500	3851	2934
0.527	9.733×10^{-2}	2.077	6.657×10^0	2.053	120 000	5185	6925
2.108	9.890×10^{-2}	–	5.926×10^0	–	15 000	2263	307
1.054	1.045×10^{-2}	3.242	6.526×10^{-1}	3.183	60 000	4384	2263
0.703	2.930×10^{-3}	3.137	1.888×10^{-1}	3.059	135 000	6441	7358
0.527	1.199×10^{-3}	3.105	7.859×10^{-2}	3.046	240 000	8614	17 269
3.514	3.292×10^{-2}	–	1.917×10^0	–	9000	1839	147
2.108	4.215×10^{-3}	4.024	2.555×10^{-1}	3.945	25 000	3015	644
1.054	2.734×10^{-4}	3.947	1.633×10^{-2}	3.967	100 000	6033	4947
0.703	5.444×10^{-5}	3.980	3.243×10^{-3}	3.988	225 000	9051	16 492
3.514	2.887×10^{-3}	–	1.254×10^{-1}	–	13 500	2404	328
2.108	2.224×10^{-4}	5.018	9.919×10^{-3}	4.967	37 500	3831	1408
1.054	6.353×10^{-6}	5.129	3.068×10^{-4}	5.015	150 000	7656	10 971
0.703	8.491×10^{-7}	4.964	4.019×10^{-5}	5.013	337 500	11 552	36 923
5.270	2.003×10^{-3}	–	7.847×10^{-2}	–	8400	1980	221
2.635	3.665×10^{-5}	5.772	1.411×10^{-3}	5.797	33 600	3819	1650
1.757	3.299×10^{-6}	5.938	1.285×10^{-4}	5.909	75 600	5657	5437
1.318	5.851×10^{-7}	6.012	2.315×10^{-5}	5.959	134 400	7496	12 730
5.270	2.004×10^{-4}	–	7.096×10^{-3}	–	11 200	2263	425
2.635	1.726×10^{-6}	6.859	5.449×10^{-5}	7.025	44 800	4526	3323
1.757	1.038×10^{-7}	6.934	3.173×10^{-6}	7.013	100 800	6647	10 886
1.318	1.412×10^{-8}	6.934	4.216×10^{-7}	7.016	179 200	8910	25 834
5.270	1.896×10^{-5}	–	4.665×10^{-4}	–	14 400	2574	843
3.514	8.074×10^{-7}	7.784	1.955×10^{-5}	7.824	32 400	3831	2784
2.635	7.903×10^{-8}	8.078	2.010×10^{-6}	7.908	57 600	5177	6653
2.108	1.365×10^{-8}	7.870	3.449×10^{-7}	7.899	90 000	6409	12 874
5.270	1.505×10^{-6}	–	3.256×10^{-5}	–	18 000	2970	1597
3.514	4.003×10^{-8}	8.945	8.438×10^{-7}	9.009	40 500	4384	5278
2.635	3.036×10^{-9}	8.965	6.434×10^{-8}	8.946	72 000	5799	12 353
2.108	4.342×10^{-10}	8.716	7.396×10^{-9}	9.694	112 500	7249	24 814
10.541	8.902×10^{-5}	–	1.660×10^{-3}	–	5500	1697	381
5.270	1.099×10^{-7}	9.662	1.764×10^{-6}	9.879	22 000	3253	2878
3.514	2.000×10^{-9}	9.882	3.188×10^{-8}	9.898	49 500	4950	9946
2.635	1.980×10^{-10}	8.038	5.285×10^{-9}	6.246	88 000	6506	23 100

Munich) for a regular mesh of square shaped elements, where h is the mesh spacing. The slopes of the top plots in Figs 3 and 4 give the convergence orders and show that with mesh refinement the errors decrease much faster if the order of the scheme is increased. Furthermore, we see that the FD scheme and the SEM are restricted to second order due to their time-stepping scheme.

Similarly, for a desired maximum error the total number of degrees of freedom, which is directly proportional to the required storage space, decreases for higher-order schemes. Or, in other words, for a given storage space higher accuracy can be reached with higher-order schemes. In the last plot of Figs 3 and 4 we demonstrate that the CPU time needed to reach a desired accuracy also decreases when using higher-order schemes, in particular on the regular meshes. For the irregular meshes, the results are less clear for rather low accuracy requirements, for example, $L^\infty > 10^{-3}$. However, if higher accuracy, for example, $L^\infty < 10^{-3}$, is desired, the higher-order schemes pay off. The comparison with FD and the SEM shows that for errors $L^\infty > 10^{-2}$ these schemes are much faster than the ADER–DG schemes. However, if very high accuracy is required, for example, $L^\infty < 10^{-3}$ these schemes are again limited in accuracy due to their time-stepping scheme of only second order. Therefore, the results of the convergence analysis clearly demonstrate the advantages of these highly accurate ADER–DG schemes.

5.2 Convergence with continuous source

In order to validate the discretization of the source terms, we study the convergence rates on the example of a fourth and sixth-order ADER–DG scheme on the regular triangular mesh (see Fig. 2). The source term is constructed such that the solution of the elastic wave eq. (2) becomes

Table 2. Convergence rates of σ_{xx} from order 2 to 10 of ADER–DG on the irregular meshes.

h	L^∞	$\mathcal{O}_{L^\infty}$	L^2	$\mathcal{O}_{L^2}$	N_d	I	CPU [s]
6.513	2.224×10^0	–	1.459×10^2	–	2976	1749	55
3.257	1.201×10^0	0.889	6.952×10^1	1.070	11 904	3496	438
1.628	2.844×10^{-1}	2.078	1.371×10^1	2.342	47 616	6991	3509
0.814	5.748×10^{-2}	2.307	2.704×10^0	2.342	190 464	13 981	28 232
6.513	7.072×10^{-1}	–	3.423×10^1	–	5952	2914	139
3.257	1.119×10^{-1}	2.660	2.517×10^0	3.765	23 808	5826	1120
1.628	1.758×10^{-2}	2.670	2.373×10^{-1}	3.407	95 232	11 651	8987
0.814	2.894×10^{-3}	2.603	2.814×10^{-2}	3.076	380 928	23 301	72 140
6.513	1.447×10^{-1}	–	1.768×10^0	–	9920	4079	315
3.257	1.111×10^{-2}	3.703	9.910×10^{-2}	4.157	39 680	8156	2526
1.628	1.054×10^{-3}	3.397	6.604×10^{-3}	3.907	158 720	16 311	20 246
0.814	8.002×10^{-5}	3.720	4.266×10^{-4}	3.952	634 880	32 621	164 634
13.026	5.288×10^{-1}	–	5.660×10^0	–	3720	2622	95
6.513	3.166×10^{-2}	4.062	1.384×10^{-1}	5.353	14 880	5243	771
3.257	1.066×10^{-3}	4.893	4.639×10^{-3}	4.899	59 520	10 485	6123
1.628	5.261×10^{-5}	4.340	1.677×10^{-4}	4.789	238 080	20 970	49 648
13.026	1.421×10^{-1}	–	7.123×10^{-1}	–	5208	3205	219
6.513	3.845×10^{-3}	5.208	1.279×10^{-2}	5.800	20 832	6408	1780
3.257	6.839×10^{-5}	5.813	2.255×10^{-4}	5.825	83 328	12 816	14 044
1.628	1.220×10^{-6}	5.809	3.892×10^{-6}	5.857	333 312	25 631	107 658
13.026	3.750×10^{-2}	–	1.569×10^{-1}	–	6944	3787	419
6.513	5.503×10^{-4}	6.091	1.197×10^{-3}	7.034	27 776	7573	3352
3.257	4.352×10^{-6}	6.982	1.009×10^{-5}	6.891	111 104	15 146	27 034
1.628	4.496×10^{-8}	6.597	9.137×10^{-8}	6.787	444 416	30 290	216 821
26.052	2.168×10^{-1}	–	4.104×10^0	–	2232	2185	111
13.026	8.565×10^{-3}	4.662	1.867×10^{-2}	7.780	8928	4370	895
6.513	4.746×10^{-5}	7.496	9.682×10^{-5}	7.591	35 712	8738	7157
3.257	2.154×10^{-7}	7.783	4.058×10^{-7}	7.898	142 848	17 476	57 415
26.052	2.481×10^{-1}	–	1.509×10^0	–	2790	2476	220
13.026	1.540×10^{-3}	7.332	3.697×10^{-3}	8.673	11 160	4952	1731
6.513	5.397×10^{-6}	8.156	7.347×10^{-6}	8.975	44 640	9903	13 779
3.257	1.040×10^{-8}	9.019	1.981×10^{-8}	8.535	178 560	19 805	108 380
26.052	3.077×10^{-2}	–	3.504×10^{-1}	–	3410	2768	374
13.026	2.393×10^{-4}	7.006	3.241×10^{-4}	10.078	13 640	5535	2981
6.513	3.265×10^{-7}	9.518	5.065×10^{-7}	9.322	54 560	11 069	23 859
3.257	4.330×10^{-10}	9.559	6.134×10^{-9}	6.368	218 240	22 136	191 180

the space–time periodic function

$$u_p(x, y, t) = u_p^0 \cdot \sin\left(\frac{2\pi}{\lambda_p^x}x\right) \cdot \sin\left(\frac{2\pi}{\lambda_p^y}y\right) \cdot \sin\left(\frac{2\pi}{T_p}t\right). \tag{57}$$

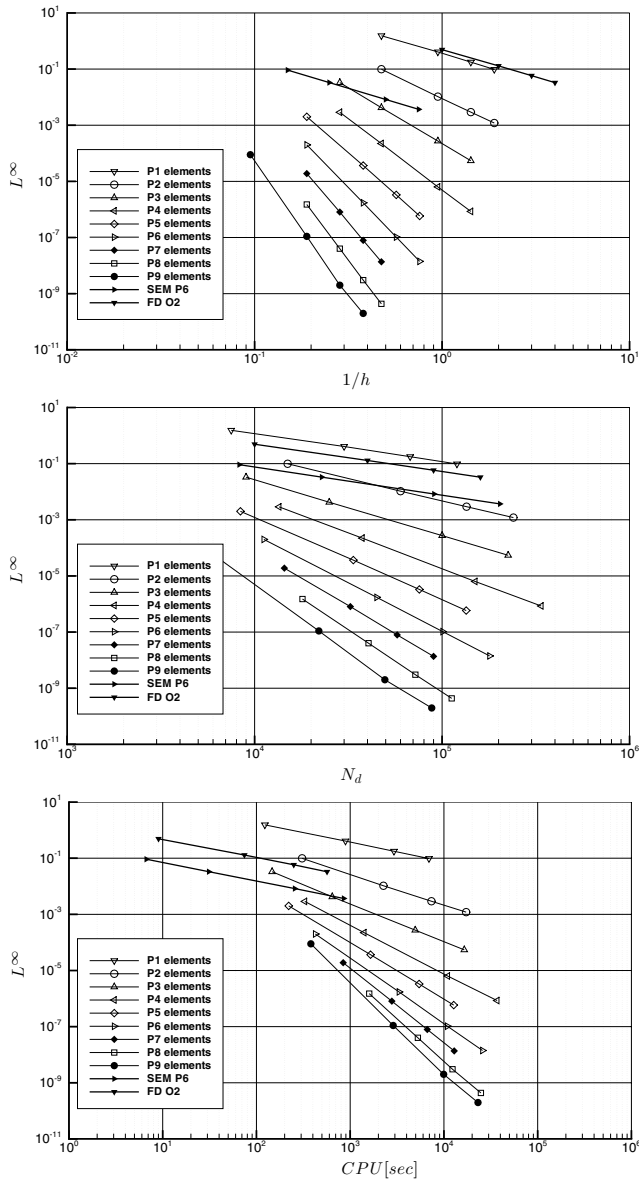For the amplitudes, spatial wave lengths and time periods of the five variables we choose the vectors

$$u_p^0 = \begin{pmatrix} 1 & 2 & 3 & 4 & 5 \end{pmatrix}^T, \tag{58}$$

$$\lambda_p^x = \lambda_p^y = \begin{pmatrix} 33\tfrac{1}{3} & 50 & 100 & 50 & 33\tfrac{1}{3} \end{pmatrix}^T, \tag{59}$$
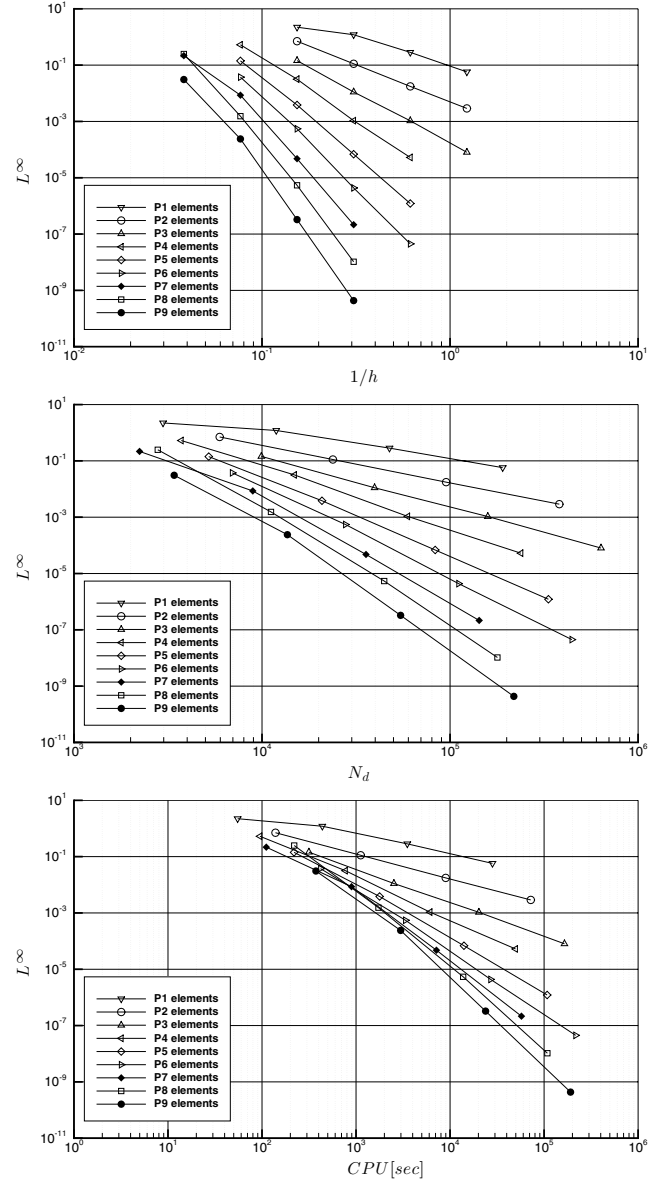
$$T_p = \begin{pmatrix} 33\tfrac{1}{3} & 50 & 100 & 10 & 5 \end{pmatrix}^T. \tag{60}$$

The spatial and temporal derivatives of the imposed solution (eq. 57) can be computed as

$$\frac{\partial}{\partial t}u_p(x, y, t) = u_p^0 \cdot \frac{2\pi}{T_p} \cdot \sin\left(\frac{2\pi}{\lambda_p^x}x\right) \cdot \sin\left(\frac{2\pi}{\lambda_p^y}y\right) \cdot \cos\left(\frac{2\pi}{T_p}t\right), \tag{61}$$

Figure 3. L^∞ error of σ_{xx} versus mesh width $1/h$, total number of degrees of freedom N_d and CPU time of ADER–DG schemes from $\mathcal{O}2 - \mathcal{O}10$ on the regular meshes.

Figure 4. L^∞ error of σ_{xx} versus mesh width $1/h$, total number of degrees of freedom N_d and CPU time of ADER–DG schemes from $\mathcal{O}2 - \mathcal{O}10$ on the irregular meshes.

$$\frac{\partial}{\partial x} u_p(x, y, t) = u_p^0 \cdot \frac{2\pi}{\lambda_p^x} \cdot \cos\left(\frac{2\pi}{\lambda_p^x} x\right) \cdot \sin\left(\frac{2\pi}{\lambda_p^y} y\right) \cdot \sin\left(\frac{2\pi}{T_p} t\right), \tag{62}$$

$$\frac{\partial}{\partial y} u_p(x, y, t) = u_p^0 \cdot \frac{2\pi}{\lambda_p^y} \cdot \sin\left(\frac{2\pi}{\lambda_p^x} x\right) \cdot \cos\left(\frac{2\pi}{\lambda_p^y} y\right) \cdot \sin\left(\frac{2\pi}{T_p} t\right), \tag{63}$$

and thus the source terms can be identified directly by inserting eqs (61), (62) and (63) into the governing equations (eq. 2) themselves.

We use the same computational domain Ω as in Section 5.1 and maximum simulation time $T = 100$. This means that the waves in the five variables oscillate for 3, 2, 1, 10 and 20 periods, respectively. Especially due to the rather high temporal frequencies of the last two variables, we expect the accuracy of the time discretization to be of great importance. We note that the initial condition is zero everywhere, which is hence the exact solution at time $t = T$.

Now, two different numerical experiments are performed. First, the scheme is implemented as given by eq. (43). Secondly, we neglect the influence of the source terms in the Cauchy-Kovalewski procedure by simply setting I_{slmon}^S to zero in eq. (43). This means that the source term is only considered on the right-hand side but not inside the wave propagation operator on the left-hand side. The CFL number is set to

Table 3. Convergence rates of v for fourth- and sixth-order ADER–DG schemes with (top) and without (bottom) including the source terms in the Cauchy-Kovalewski procedure.

			ADER–DG $\mathcal{O}4$				
h	L^∞	$\mathcal{O}_{L\infty}$	L^2	$\mathcal{O}_{L^2}$	N_d	I	CPU [s]
5.270	3.713×10^{-2}	–	1.243×10^{-0}	–	4000	648	441
2.635	6.821×10^{-4}	5.8	1.942×10^{-2}	6.0	16 000	1259	3315
1.318	1.891×10^{-5}	5.2	4.113×10^{-4}	5.6	64 000	2448	24 867
1.054	5.801×10^{-6}	5.3	1.294×10^{-4}	5.2	100 000	3099	48 894
5.270	3.363×10^{-2}	–	1.190×10^{-0}	–	4000	840	76
2.635	1.000×10^{-3}	5.1	2.560×10^{-2}	5.5	16 000	1680	609
1.318	1.004×10^{-4}	3.3	3.569×10^{-3}	2.8	64 000	3361	4831
1.054	5.844×10^{-5}	2.4	2.292×10^{-3}	2.0	100 000	4201	9479

			ADER–DG $\mathcal{O}6$				
h	L^∞	$\mathcal{O}_{L\infty}$	L^2	$\mathcal{O}_{L^2}$	N_d	I	CPU [s]
10.541	7.556×10^{-3}	–	2.217×10^{-1}	–	2100	500	1200
5.270	2.376×10^{-4}	5.0	7.600×10^{-3}	4.9	8400	990	9750
2.635	7.782×10^{-7}	8.3	1.720×10^{-5}	8.8	33 600	1900	73 814
1.757	4.752×10^{-8}	6.9	9.750×10^{-7}	7.1	75 600	2900	248 346
10.541	1.614×10^{-2}	–	$5.010 \times 10^{+1}$	–	2100	661	51
5.270	6.459×10^{-4}	4.6	2.153×10^{0}	4.5	8400	1320	410
2.635	1.301×10^{-4}	2.3	4.536×10^{-1}	2.2	33 600	2641	3281
1.757	6.320×10^{-5}	1.8	2.231×10^{-1}	1.8	75 600	3960	11 355

70 per cent of the stability limit $\frac{1}{2N+1}$ of Runge-Kutta DG schemes if the source term is neglected in the Cauchy-Kovalewski procedure and to 50 *per cent* of this stability limit if the source term is included.

In Table 3 the errors in L^∞ and L^2 norm of the vertical velocity v are given as a function of h. The corresponding numerical convergence orders $\mathcal{O}_{L\infty}$ and $\mathcal{O}_{L^2}$ are determined by two successively refined meshes. Furthermore, we present the total number N_d of degrees of freedom, the number I of required iterations and the CPU time in seconds.

We clearly see from Table 3 that the designed fourth and sixth order of accuracy has been reached, respectively, in the case where we correctly include the source term in the Cauchy-Kovalewski procedure. If we neglect it, only second order of accuracy is retrieved globally. This result clearly emphasizes the importance of highly accurate time discretization for time-dependent problems. However, the computational cost of incorporating the source term correctly is very high.

6 NUMERICAL EXAMPLES

In this Section we present three numerical examples in order to demonstrate the performance and flexibility of the proposed ADER–DG scheme.

The first is the well-known Lamb's Problem and allows us to validate the correctness of including a vertical force as a point source and the formulation of the free surface boundary condition of a homogeneous elastic half-space, as an analytical reference solution is available. In the second example we reproduce the results published in the book of LeVeque (2002) in order to show how large contrasts in material parameters of a heterogeneous medium can be easily handled. Hereby we clearly demonstrate that higher-order schemes pay off, when high resolution results are required.

In the third example we apply our scheme to the case of global seismic wave propagation, where the advantages of flexible, triangular meshes are presented. Using an unstructured mesh we can easily overcome the problem of decreasing mesh spacing towards the Earth's centre that usually arises when working with regular, structured grids, for example, using FD methods. In addition, we adjust the mesh spacing in a way to optimally make use of the CFL criterion, that is, larger elements are used in zones of higher velocity, where the expected wavelengths are larger and thus element sizes can be increased.

6.1 Lamb's Problem

A classical test case to validate the implementation of free surface boundary conditions and point sources is Lamb's Problem (Lamb 1904), consisting in a vertical (with respect to the surface) point force acting *on* the free surface. The solution of Lamb's Problem for a plane surface can be computed analytically, see for example, (Pilant 1979) and can hence be used to evaluate numerical results. In this paper we use the FORTRAN code `EX2DDIR` of Berg *et al.* (1994) to compute the exact solution of the seismic 2-D response from a vertical directional point
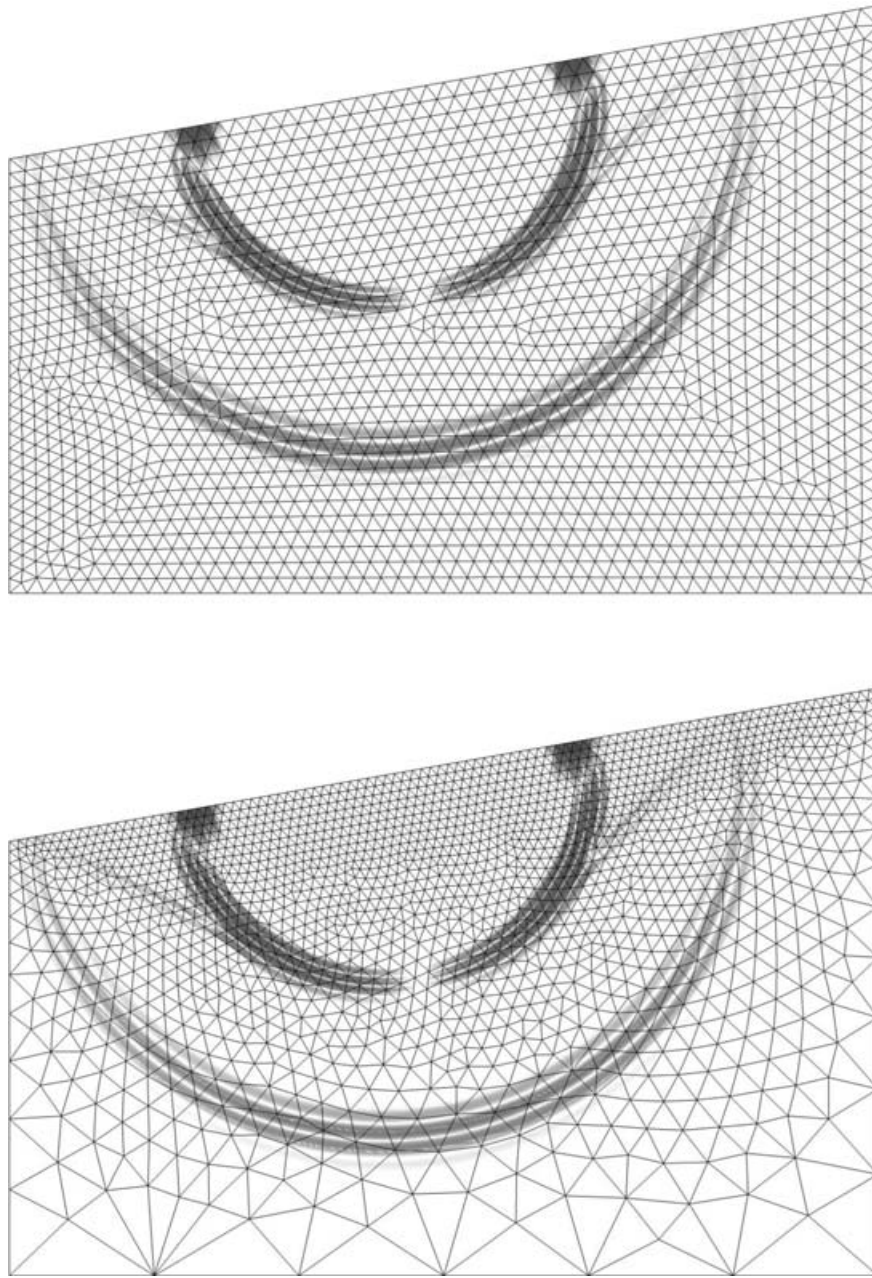
Figure 5. Vertical velocity v at $t = 0.6$ s for Lamb's problem. ADER–DG $\mathcal{O}10$ scheme on a regular (top) and refined (bottom) triangular mesh.

source in an elastic half space with a free surface. The code EX2DDIR is based on the Cagniard-de Hoop technique (de Hoop 1960) and allows the use of an arbitrary source time function for displacements or velocities. Considering the accuracy of a numerical method and the correct treatment of sources and free boundary conditions Lamb's Problem poses a challenging test case in particular for the non-dispersive Rayleigh waves propagating along a plane free surface of an homogeneous half space.

The set-up of the physical problem is chosen as in the paper of Komatitsch & Vilotte (1998), who solved this problem using the SEM, see for example, (Komatitsch & Tromp 1999, 2002).

We use a homogeneous elastic medium with a P-wave velocity of $c_p = 3200 \, \mathrm{m \, s^{-1}}$, an S-wave velocity of $c_s = 1847.5 \, \mathrm{m \, s^{-1}}$ and a mass density of $\rho = 2200 \, \mathrm{kg \, m^{-3}}$. The numerical model with origin $(0, 0)$ at the left bottom corner is 4000 m wide and has a height of 2000 m on the left boundary. The tilt angle of the free surface is $\phi = 10°$. The directional point source, acting as a force perpendicular to this tilted surface, is located at the free surface at $\vec{x}_s = (1720.00, \ 2303.28)^T$. The two receivers are located at $(2694.96, 2475.18)$ and $(3400.08, 2599.52)$ such that their distances from the source along the surface are 990 m and 1706 m, respectively. On the left, right and bottom boundaries of the model we use then absorbing boundary conditions as described in Section 4.1. We use a triangular mesh such that the left and right boundaries of the model are discretized by 30 triangle edges and the bottom and top boundaries by 50 triangles, similar to Komatitsch & Vilotte (1998). The resulting mesh is displayed in Fig. 5 (top) and consists of 3416 triangles. In order to avoid undesired effects of possibly reflected wave energy

at the right model boundary, we extended the mesh up to a width of 4700 m for the numerical computations. The source time function that specifies the temporal variation of the point source is a Ricker wavelet given by

$$S^T(t) = a_1 \left(0.5 + a_2(t - t_D)^2\right) e^{a_2(t-t_D)^2}, \tag{64}$$

where $t_D = 0.08$ s is the source delay time and $a_1 = -2000\,\text{kg}\,\text{m}^{-2}\,\text{s}^{-2}$ and $a_2 = -(\pi f_c)^2$ are constants determining the amplitude and frequency of the Ricker wavelet of central frequency $f_c = 14.5$ Hz.

The final resulting source vector $S_p(x, y, t)$ acting on the governing PDE (1) or (2), respectively, taking into account also the tilt angle ϕ is

$$S_p(x, y, t) = \begin{pmatrix} 0 & 0 & 0 & -\sin(\phi) & \cos(\phi) \end{pmatrix}^T \cdot \frac{S^T(t)}{\rho} \cdot \delta(\vec{x} - \vec{x}_s). \tag{65}$$

The wave propagation is simulated until time $T_{\text{end}} = 1.3$ s when all waves have already passed the two receivers. For the results shown in this paper, a tenth-order ADER–DG $\mathcal{O}10$ scheme with a Courant number of CFL = 0.5 is used. In order to reach the final simulation time T_{end} we need 5915 time steps. We then perform the same simulation on a refined mesh, where the mesh spacing is gradually decreasing towards the free surface, see Fig. 5 (bottom). This problem-adapted mesh helps to resolve surface effects, such as the Rayleigh waves, with higher accuracy and requires 8836 time steps to reach T_{end}. In Fig. 5 we present the snapshots of the vertical velocity component v of the seismic wavefield at $t = 0.6$ s on a regular (top) and refined (bottom) triangular mesh. We remark that the total number of triangles used in both simulations is the same. Visually, there is a perfect match between both numerical solutions. In Fig. 6 we present the unscaled seismograms obtained from our numerical simulations, as recorded by receiver 1 and 2, respectively, together with the analytical solution provided by EX2DDIR. The analytical and numerical solutions match extremely well, such that the lines basically are not distinguishable on this scale. Therefore, the residuals are also plotted and are amplified by a factor of 10 in order to make differences more visible. The maximum relative error on the regular mesh remains always less than 1 per cent, however, it is considerably smaller on the surface-refined mesh where it is about 0.3 per cent. We conclude from this example that correctly including the source terms in the Cauchy-Kovalewski procedure is also beneficial with respect to accuracy in the context of point sources. In particular, for point sources the additional computational effort is very small, as the Cauchy-Kovalewski procedure with source terms appears only in the triangle, where the point sources is located. In addition, the accurate solution of Lamb's problem with the ADER–DG method confirms that the implementation of free surface boundary conditions as suggested in 4.2 leads to the correct physical behaviour of elastic surface waves.

6.2 Stiff inclusion

The following numerical example is based on a test case given by LeVeque (2002) in Chapter 22.7. An initial plane P wave travels through a heterogeneous elastic medium. The medium consists of two different materials where in an outer solid material of extent $\Omega_o = [-1, 1] \times [-0.5.0.5]$ is embedded another, stiffer, elastic material of size $\Omega_i = [-0.5, 0.5] \times [-0.1.0.1]$. The elastic properties of the outer material are $\rho_o = 1$, $\lambda_o = 2$, and $\mu_o = 1$, whereas the inner material has the properties $\rho_i = 1$, $\lambda_i = 200$, and $\mu_i = 100$. Therefore, we have to deal with a large jump of the physical parameters at the interface between the two materials. The wave speeds of both P and S waves inside the stiffer material are 10 times larger than in the outer medium.

At the left and right boundaries ($x = \pm 1$) of Ω_o we implemented absorbing boundaries, whereas at the top and bottom boundaries ($y = \pm 0.5$) we use a free surface boundary condition, where the normal stress σ_{yy} and the shear stress σ_{xy} must vanish.

The initial condition is given by

$$u_p^0 = u_p(\vec{x}, 0) = R_{p5}^{A_n} \exp\left(-\frac{1}{2}\frac{(x - x_0)^2}{\sigma^2}\right), \tag{66}$$

with $\vec{n} = (1, 0)^T$, $x_0 = -0.8$ and standard deviation $\sigma = 0.01$, which represents a plane P wave of Gaussian shape travelling in x-direction. Initially, the centre of the plane wave is located at $x = -0.8$. Due to the free surface boundary condition at $y = \pm0.5$, surface waves develop right from the beginning of the simulation. When the planar wave hits the stiffer material of the inclusion at $x = -0.5$ at time $t = 0.15$, the elastic waves travel with 10 times higher velocities through the inclusion where they are reflected each time they hit either of the boundaries at $x = \pm 0.5$. Therefore, the inclusion starts to vibrate, radiating waves of small amplitude into the outer material. Similar to LeVeque (2002) we use a non-linear colour scale in order to visualize also these waves with small amplitude.

In Fig. 7 we show two snapshots of the component σ_{xx} of the resulting wavefield at simulation time $t = 0.3$. In the top Figure, we used an ADER–DG $\mathcal{O}4$ scheme that uses 10 degrees of freedom per element. The corresponding mesh is constructed by using 200×100 squares in x- and y-direction, respectively, where each square is split into 4 similar triangles as shown in Fig. 2a). Therefore, the total number of triangles in the mesh is 80 000.

In the bottom snapshot of Fig. 7, we used an ADER–DG $\mathcal{O}6$ scheme. The mesh spacing is now increased such that we only use 100×50 squares in x- and y-direction, respectively. Therefore, the total number of triangles is only 20 000 but due to the higher order of the scheme we now have 21 degrees of freedom per triangle, which finally roughly leads to half of the total number of degrees of freedom for the sixth-order scheme. Comparing the measured CPU times of the fourth and the sixth-order method we indeed get a two times lower CPU time for the computation with the ADER–DG $\mathcal{O}6$ scheme compared to the ADER–DG $\mathcal{O}4$ method. Visually comparing the snapshots in Fig. 7, one can hardly see any difference between the two results. In both cases all features of the solution are resolved equally well. Comparing our
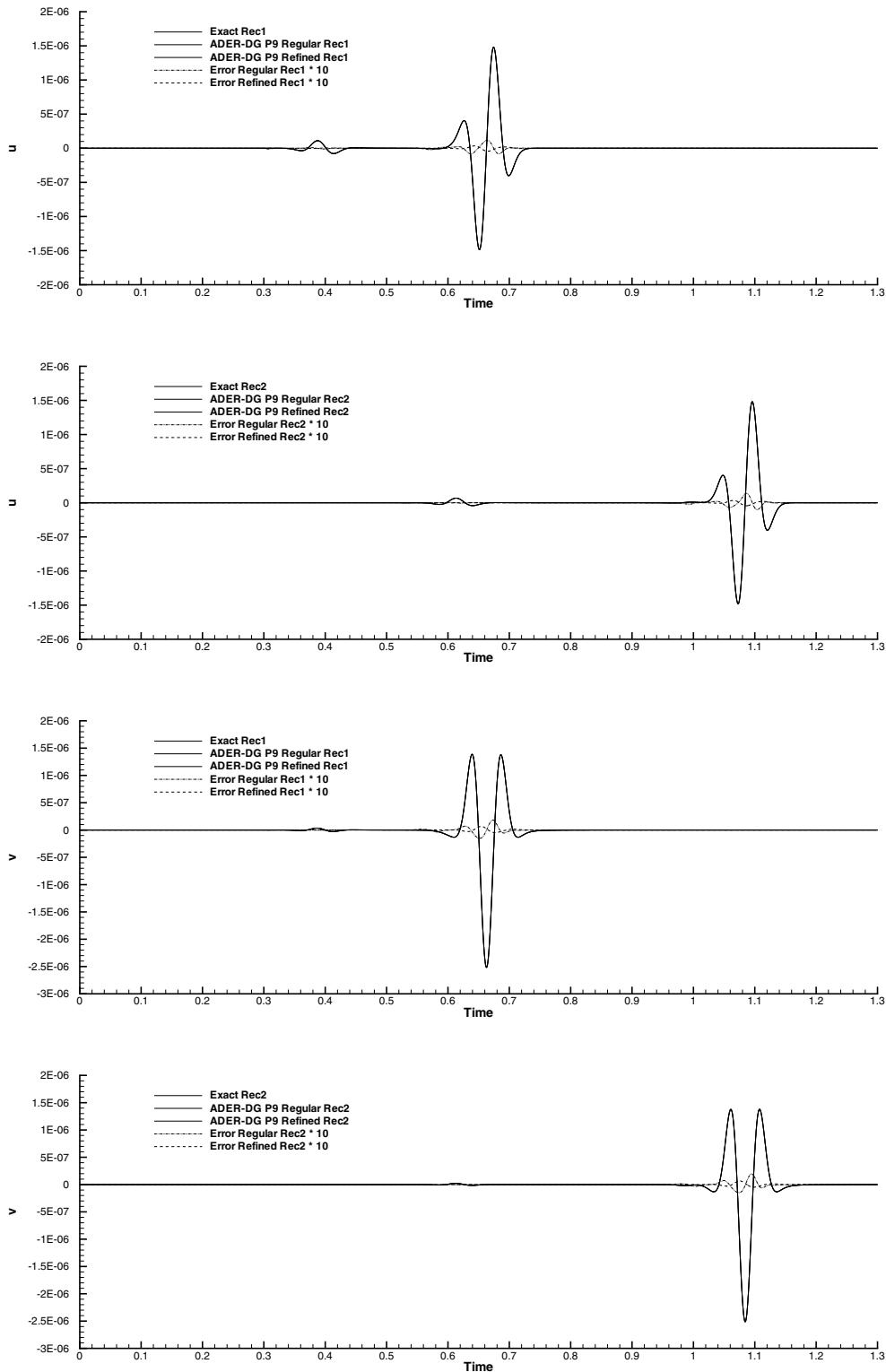
Figure 6. Seismograms of the normal and tangential velocity components w.r.t. the surface at the two receivers 1 and 2 for Lamb's problem.

results qualitatively we get an excellent agreement with the solution of LeVeque (2002), who used a slightly different initial condition and a second-order FV scheme on a 600×300 Cartesian grid. We note that for visualization of the results, the numerical solution is shown on a much finer grid than the one used for the computations in order to exploit the subcell resolution of the ADER–DG schemes. At these visualization vertices the numerical solution is evaluated according to eq. (9).

From these results we conclude that for this example with strong jumps in the material properties the ADER–DG method behaves very robustly. Furthermore, confirming the results already obtained in the numerical convergence analysis in Section 5, we can see that in order to reach a certain resolution, less CPU time and also less memory is needed for higher-order methods.
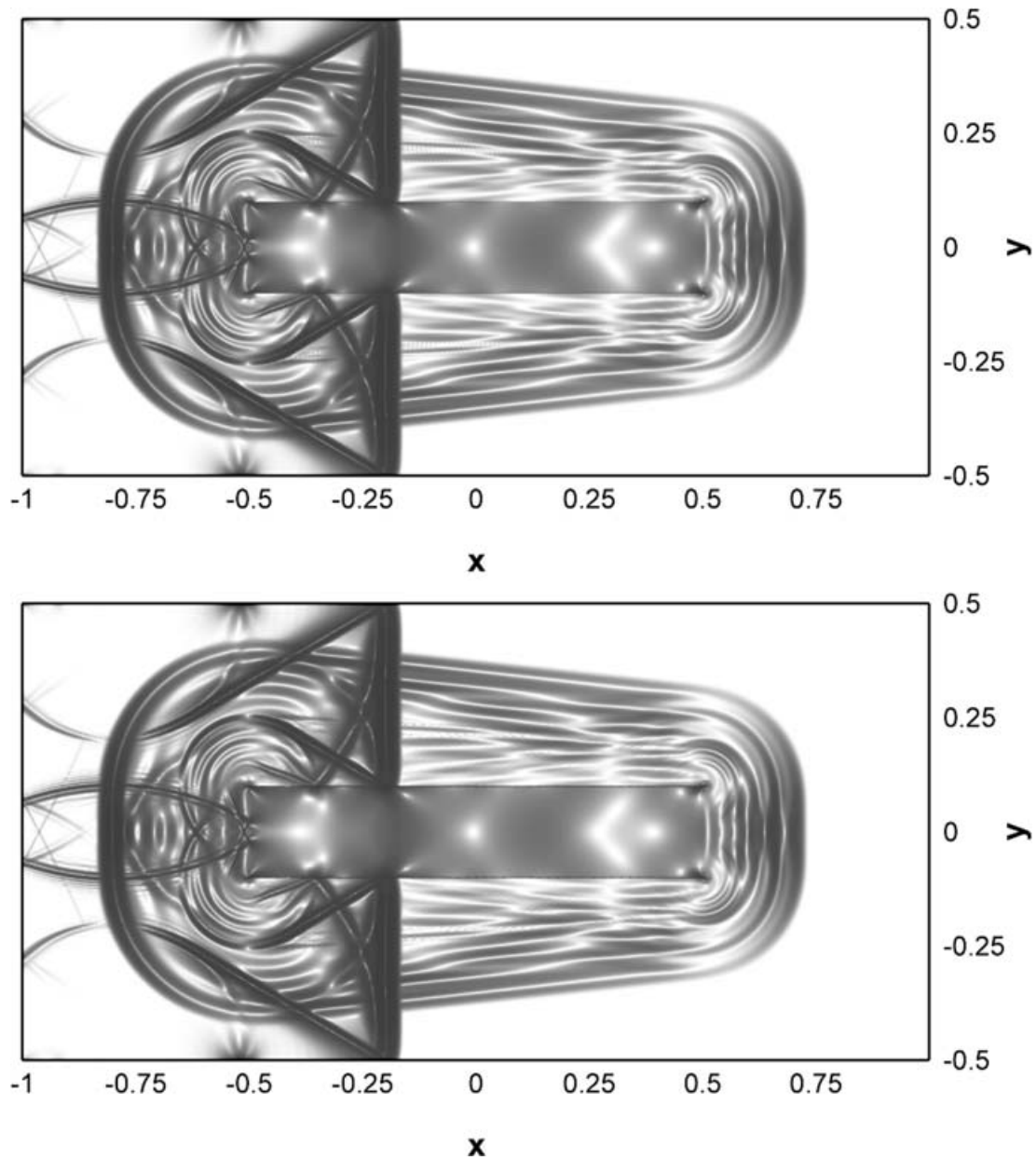
Figure 7. Stress component σ_{xx} at $t = 0.3$ for the inclusion test case. ADER–DG $\mathcal{O}4$ scheme with $4 \cdot 200 \times 100$ triangles (top), ADER–DG $\mathcal{O}6$ scheme with $4 \cdot 100 \times 50$ triangles (bottom).

6.3 Global seismology

In the second example we present the results of a global simulation of seismic waves, which is often problematic for FD methods due to the generation of an appropriate mesh. As FD schemes rely on a certain regularity of the mesh, spherical coordinates are often used. However, towards the centre of the model, the mesh spacing decreases with depth such that the allowed time step decreases drastically and thus practical computations become difficult. Hence, regular meshes have to be recoarsened successively with depth and interpolation procedures are required to handle hanging nodes like in (Thomas *et al.* 2000). Therefore, FD methods often are restricted to spherical sections, see for example, (Igel 1999; Igel *et al.* 2002).

SEM overcomes this problem using the cubed-sphere approach as shown in (Komatitsch & Tromp 2002). Here the mesh is designed especially for the radial structure of PREM.

The proposed ADER–DG scheme on triangular meshes uses a different approach and demonstrates a higher flexibility concerning difficult geometries. Therefore, a circular geometry as needed for the discretization of the radially symmetric PREM of Dziewonski & Anderson (1981) does not impose any problems. As shown in Fig. 8(a) triangular mesh can be built that respects the radial symmetry of the different layers of the PREM. Furthermore, the local mesh width can be adapted proportional to the local seismic waves velocity. Hence, we chose larger triangular elements in areas with high wave speeds, for example, in the lower mantle and small elements in low-velocity zones, such as close
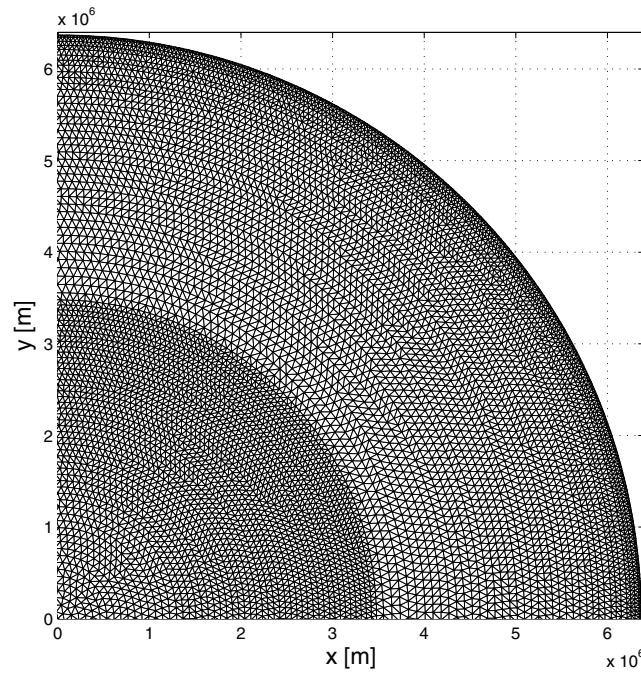
Figure 8. Top right quarter of the well adapted, velocity-dependent triangular mesh constructed for the simulation of global elastic wave propagation using PREM.

to the surface or below the core-mantle boundary, where seismic wave speeds decrease dramatically. This way, the time step according to the local CFL condition is used in an optimal sense.

We use an explosive source at location $(x_s, y_s) = (0, 6200)$ km, that is, 171 km below the Earth's surface. The seismograms on the surface are recorded on 37 receivers located at positions from $(x_{r_1}, y_{r_1})=(0, 6371)$ km until $(x_{r_{37}}, y_{r_{37}})=(0, -6371)$ km with equidistant epicentral distances $\Delta_i = (i - 1) \cdot 5°$, $i = 1, \ldots, 37$. In Fig. 9 we show the wavefield of the vertical velocity component w at three different times, after 300, 600 and 900 seconds together with the seismograms of the vertical and transverse velocity components with respect to the Earth's surface. Again we use a non-linear colour scale for the snapshots and amplification in the seismograms to visualize small amplitudes. At $t = 300$ s a strong reflection of P and S waves at the core-mantle boundary can be observed. At time $t = 600$ s the direct P wave passes in inner core creating S waves at the interface between outer and inner core. When the direct P wave has passed the Earth's inner and outer core at $t = 900$ s it leaves the inner, stiffer core vibrating similar to the observations in Section 6.2. Furthermore, the shadowing effect of the core with respect to the direct wave can be seen.

Additional 19 receivers with coordinates $(x_{r_i}, y_{r_i}) = (-6371 + i \cdot 637.1, 0)$ km, $i = 1, \ldots, 19$ are placed on a horizontal line through the Earth centre in order to register the shear stress component σ_{xy} at different depths. As shown in Fig. 9(f), no shear stress component or spurious S waves appear in the liquid outer core. We note that we do not compare the obtained results with reference solutions, as we only want to demonstrate the performance of the applied ADER–DG $\mathcal{O}6$ scheme on this problem. However, we state that with the proposed ADER–DG scheme of high order in space and time we still can resolve very fine features of the global wavefield on rather coarse meshes, even after long simulation times when waves have propagated many wavelengths.

7 DISCUSSION AND CONCLUSIONS

We presented the mathematical details, convergence properties and applications of a new numerical approach, termed ADER–DG method, for the solution of the elastic wave equations on unstructured triangular meshes. The scope of this work has been to introduce and extend this arbitrarily high-order accurate numerical method, originally developed in the field of computational fluid dynamics, to the community of numerical seismology in order to demonstrate its advantages to commonly used methods. As the amount and quality of information of the Earth interior or of structures and properties of hydrocarbon reservoirs are growing rapidly and are becoming more detailed, it is of uttermost importance to develop computational tools that can use such models to compute highly accurate synthetic seismograms. In this work we described a numerical method that helps to reduce the numerical approximation error as much as possible, such that deviations from measured data have to originate basically from incorrect model parametrization. Therefore, in our opinion the new ADER–DG method can play a significant role for understanding the processes of wave propagation in complex, heterogeneous media as well as for model validation. In contrast to existing methods, the proposed ADER–DG scheme retains its high-order accuracy and space and time even on unstructured meshes, which makes it particularly suited for problems of complicated geometry. We clearly could show that due to its subcell resolution very coarse meshes can be used, which reduce the amount of required computer storage and allow for large time steps. Therefore, the computational

(a) $t = 300$s

(d)

(b) $t = 600$s

(e)

(c) $t = 900$s

(f)
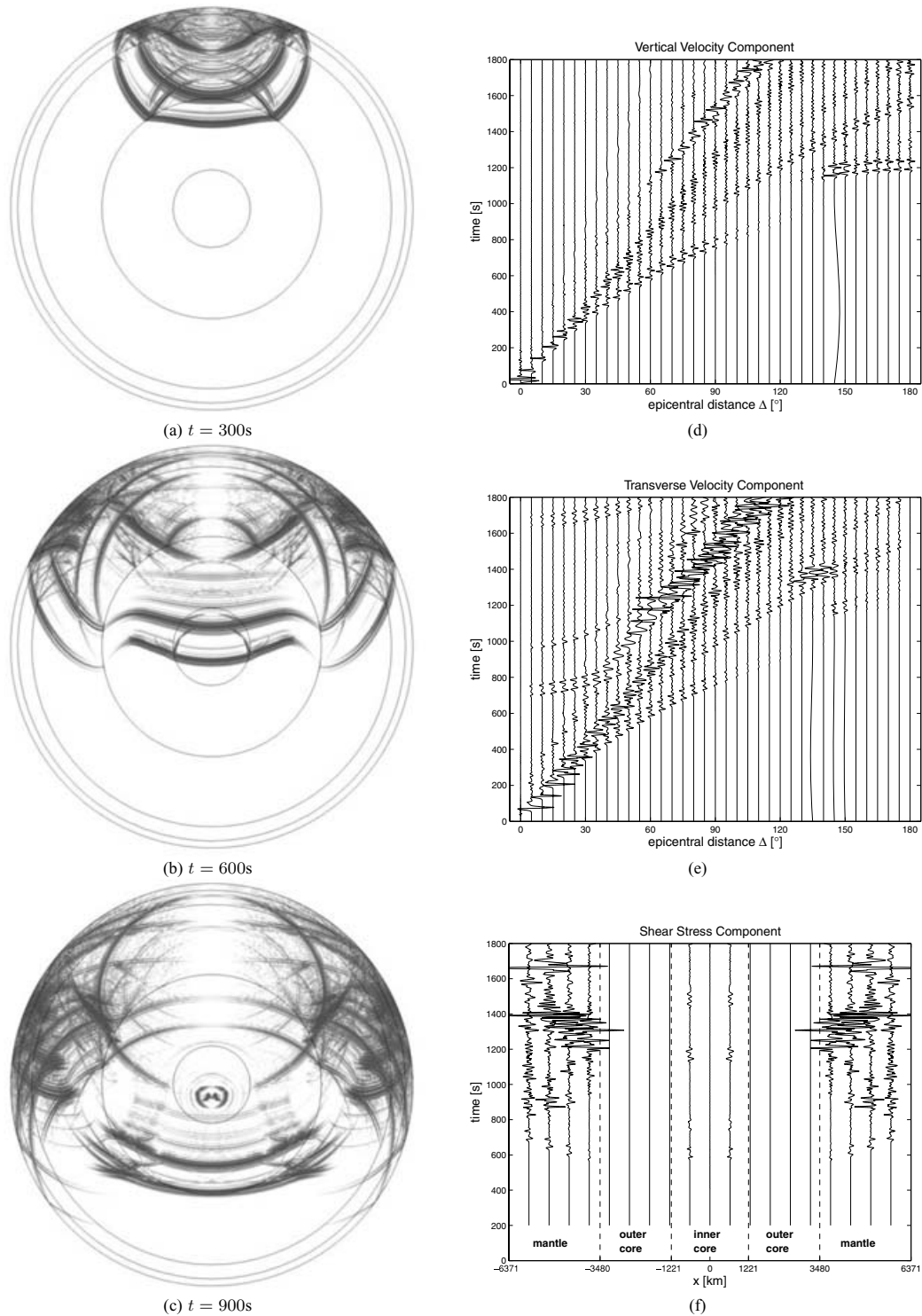
Figure 9. Snapshots of the velocity component w of the seismic wave field for the 2-D PREM after (a) $t = 300$ s, (b) $t = 600$ s and (c) $t = 900$ s. Seismograms of the d) vertical and e) transverse velocity component with respect to the Earth's surface. (f) The shear stress σ_{xy} recorded at different depths. Note that in the liquid outer core, the recorded shear stress is exactly zero.

efficiency of ADER–DG schemes increases with the order of accuracy. With the ongoing, rapidly growing computer power, the arbitrary high order of ADER–DG schemes provide a method that will automatically follow these developments, such that we will always be able to reach machine precision just by increasing the desired order of accuracy. In addition, we demonstrated that strong material heterogeneities, which often lead to problems in staggered finite difference schemes, can easily be handled, if element interfaces are aligned with the material boundary, as discontinuities of the numerical approximation are allowed between two adjacent elements.

REFERENCES

Aki, K. & Richards, P.G., 2002. *Quantitative Seismology*, University Science Books, Sausalito, California.

Atkins, H. & Shu, C.W., 1998. Quadrature-free implementation of the Discontinuous Galerkin method for hyperbolic equations, *AIAA Journal,* **36,** 775–782.

Bedford, A. & Drumheller, D.S., 1994. *Elastic Wave Propagation*, Wiley, Chichester, UK.

Bérenger, 1994. A Perfectly Matched Layer for the absorption of electromagnetic waves, *J. Comput. Phys.,* **114,** 185–200.

Berg, P., If, F., Nielsen, P. & Skovgaard, O., 1994. Analytical reference solutions, in *Modeling the earth for oil exploration*, pp. 421–427, ed. Helbig, K., Pergamon Press, Brussels.

Butcher, J.C., 1987. *The Numerical Analysis of Ordinary Differential Equations: Runge-Kutta and General Linear Methods*, Wiley, New York.

Carcione, J.M., 1994. The wave equation in generalised coordinates, *Geophysics,* **59,** 1911–1919.

Cockburn, B. & Shu, C.W., 1989. TVB Runge-Kutta local projection discontinuous Galerkin finite element method for conservation laws II: general framework, *Math. Comp.,* **52,** 411–435.

Cockburn, B. & Shu, C.W., 1991. The Runge-Kutta local projection P1-Discontinuous Galerkin finite element method for scalar conservation laws, *Mathematical Modelling and Numerical Analysis,* **25,** 337–361.

Cockburn, B. & Shu, C.W., 1998. The Runge-Kutta discontinuous Galerkin method for conservation laws V: multidimensional systems, *J. Comput. Phys.,* **141,** 199–224.

Cockburn, B., Lin, S.Y. & Shu, C.W., 1989. TVB Runge-Kutta local projection discontinuous Galerkin finite element method for conservation laws III: one dimensional systems, *J. Comput. Phys.,* **84,** 90–113.

Cockburn, B., Hou, S. & Shu, C.W., 1990. The Runge-Kutta local projection discontinuous Galerkin finite element method for conservation laws IV: the multidimensional case, *Math. Comp.,* **54,** 545–581.

Cockburn, B., Karniadakis, G.E. & Shu, C.W., 2000. *Discontinuous Galerkin Methods, Theory, Computation and Applications*, LNCSE, **11,** Springer, Berlin.

Collino, F. & Tsogka, C., 2001. Application of the PML absorbing layer model to the linear elastodynamic problem in anisotropic heterogeneous media, *Geophysics,* **66,** 294–307.

Courant, R., Friedrichs, K.O. & Lewy, H., 1928. Über die partiellen Differenzialgleichungen der mathematischen Physik, *Mathematische Annalen,* **100,** 32–74.

de Hoop, A.T., 1960. A modification of Cagniard's method for solving seismic pulse problems, *Appl. Sci. Res.,* **B8,** 349–356.

Dubiner, M., 1991. Spectral methods on triangles and other domains, *Journal of Scientific Computing,* **6,** 345–390.

Dumbser, M., 2005. Arbitrary High Order Schemes for the Solution of Hyperbolic Conservation Laws in Complex Domains, Shaker Verlag, Aachen.

Dumbser, M. & Munz, C.D., 2005a. ADER Discontinuous Galerkin schemes for Aeroacoustics, *Comptes Rendus-Mecanique,* **333,** 683–687.

Dumbser, M. & Munz, C.D., 2005b. Arbitrary High Order Discontinuous Galerkin Schemes, in *Numerical Methods for Hyperbolic and Kinetic Problems*, pp. 295–333, eds Cordier, S., Goudon, T., Gutnic, M. & Sonnendrucker, E., IRMA Series in Mathematics and Theoretical Physics, EMS Publishing House, Zürich.

Dumbser, M., Schwartzkopff, T. & Munz, C.D., 2005. Arbitrary High Order Finite Volume Schemes for Linear Wave Propagation, to appear in *Notes on Numerical Fluid Mechanics and Multidisciplinary Design (NNFM)*, Springer, Heidelberg.

Dziewonski, A.M. & Anderson, D.L., 1981. Preliminary reference Earth model, *Phys. Earth planet. Inter.,* **25,** 297–356.

Fornberg, B., 1996. *A Practical Guide to Pseudospectral Methods*, Cambridge University Press, Cambridge, UK.

Hempel, D., 1995. Isotropic refinement and recoarsening in 2 dimensions, Technical Report, IB 223-95 A 35, DLR.

Hughes, T.J.R., 1987. *The Finite Element Method–Linear Static and Dynamic Finite Element Analysis*, Prentice Hall, Englewood Cliffs, NJ, USA.

Igel, H., 1999. Wave propagation in three-dimensional spherical sections by the Chebyshev spectral method, *Geophys. J. Int.,* **136,** 559–566.

Igel, H., Mora, P. & Riollet, B., 1995. Anisotropic wave propagation through finite-difference grids, *Geophysics,* **60,** 1203–1216.

Igel, H., Nissen-Meyer, T. & Jahnke, G., 2002. Wave propagation in 3D spherical sections. Effects of subduction zones, *Phys. Earth planet. Int.,* **132,** 219–234.

Käser, M. & Igel, H., 2001a. Numerical simulation of 2D wave propagation on unstructured grids using explicit differential operators, *Geophys. Prospect.,* **49,** 607–619.

Käser, M. & Igel, H., 2001b. A comparative study of explicit differential operators on arbitrary grids, *J. Comput. Acoustics,* **9,** 1111–1125.

Komatitsch, D. & Tromp, J., 1999. Introduction to the spectral-element method for 3-D seismic wave propagation, *Geophys. J. Int.,* **139,** 806–822.

Komatitsch, D. & Tromp, J., 2002. Spectral-element simulations of global seismic wave propagation—I. Validation, *Geophys. J. Int.,* **149,** 390–412.

Komatitsch, D. & Tromp, J., 2003. A perfectly matched layer absorbing boundary condition for the second-order seismic wave equation, *Geophys. J. Int.,* **154,** 146–153.

Komatitsch, D. & Vilotte, J.P., 1998. The spectral-element method: an efficient tool to simulate the seismic response of 2D and 3D geological structures, *Bull. seism. Soc. Am.,* **88,** 368–392.

Lamb, H., 1904. On the propagation of tremors over the surface of an elastic solid, *Phil. Trans. R. Soc. Lond., Ser. A.,* **203,** 1–42.

Levander, A.R., 1988. Fourth-order finite difference P-SV seismograms, *Geophysics,* **53,** 1425–1436.

LeVeque, R.L., 2002. *Finite Volume Methods for Hyperbolic Problems*, Cambridge University Press, Cambridge, UK.

Madariaga, R., 1976. Dynamics of an expanding circular fault, *Bull. seism. Soc. Am.,* **65,** 163–182.

Meister, A. & Struckmeier, J., 2002. *Hyperbolic Partial Differential Equations: Theory, Numerics and Applications*, Vieweg, Braunschweig.

Moczo, P., Kristek, J., Vavrycuk, V., Archuleta, R.J. & Halada, L., 2002. 3D heterogeneous staggered-grid finite-difference modeling of seismic motion with volume harmonic and arithmetic averaging of elastic moduli and densities, *Bull. seism. Soc. Am.,* **92,** 3042–3066.

Mora, P., 1989. Modeling anisotropic seismic waves in 3-D, *59th Ann. Int. Mtg Exploration Geophysicists, expanded abstracts,* 1039–1043.

Patera, A.T., 1984. A spectral-element method for fluid dynamics: laminar flow in a channel expansion, *J. Comput. Phys.,* **144,** 45–58.

Pilant, W.L., 1979. *Elastic Waves in the Earth*, Elsevier Scientific Publishing.

Priolo, E., Carcione, J.M. & Seriani, G., 1994. Numerical simulation of interface waves by high-order spectral modeling techniques, *J. acoust. Soc. Am.,* **95,** 681–693.

Reed, W.H. & Hill, T.R., 1973. Triangular mesh methods for the neutron transport equation, Technical Report, LA-UR-73-479, Los Alamos Scientific Laboratory.

Schwartzkopff, T., Munz, C.D. & Toro, E.F., 2002. ADER: a high-order Approach for Linear Hyperbolic Systems in 2D, *J. Sci. Comput.,* **17,** 231–240.

Schwartzkopff, T., Dumbser, M. & Munz, C.D., 2004. Fast high order ADER schemes for linear hyperbolic equations, *J. Comput. Phys.,* **197,** 532–539.

Schwarz, H.R., 1988. *Finite Element Methods*, Academic Press, London.

Seriani, G., 1998. 3-D large-scale wave propagation modeling by a spectral-element method on a Cray T3E multiprocessor, *Comput. Methods Appl. Mech. Eng.,* **164,** 235–247.

Tessmer, E., 1995. 3-D Seismic modelling of general material anisotropy in the presence of the free surface by a Chebyshev spectral method, *Geophys. J. Int.,* **121,** 557–575.

Tessmer, E. & Kosloff, D., 1994. 3-D Elastic modelling with surface topography by a Chebyshev spectral method, *Geophysics,* **59,** 464–473.

Thomas, C., Igel, H., Weber, M. & Scherbaum, F., 2000. Acoustic simulation of *P*-wave propagation in a heterogeneous spherical earth: numerical method and application to precursor waves to PKPdf, *Geophys. J. Int.,* **141,** 307–320.

Thompson, L.L. & Pinsky, P., 1996. A space-time finite element method for structural acoustics in infinite domains. Part 1: formulation, stability and convergence, *Comp. Meth. Appl. Mech. Eng.,* **132,** 195–227.

Titarev, V.A. & Toro, E.F., 2002. ADER: arbitrary high order Godunov approach, *J. Sci. Comput.,* **17,** 609–618.

Toro, E.F., Millington, A.C. & Nejad, L.A., 2001. Towards very high order Godunov schemes, in *Godunov Methods; Theory and applications*, Kluwer Academic Plenum Publishers, Oxford, 907–940.

Toro, E.F. & Titarev, V.A., 2002. Solution of the generalized Riemann problem for advection-reaction equations, *Proc. Roy. Soc. London,* **458,** 271–281.

Virieux, J., 1984. SH-wave propagation in heterogeneous media: velocity-stress finite-diffe4ence method, *Geophysics,* **49,** 1933–1942.

Virieux, J., 1986. P-SV wave propagation in heterogeneous media: Velocity-stress finite-difference method, *Geophysics,* **51,** 889–901.